RECLAMATION

Managing Water in the West

Desalination and Water Purification Research and Development Program Report No. 161

Static Mixing Spacers for Spiral Wound Modules

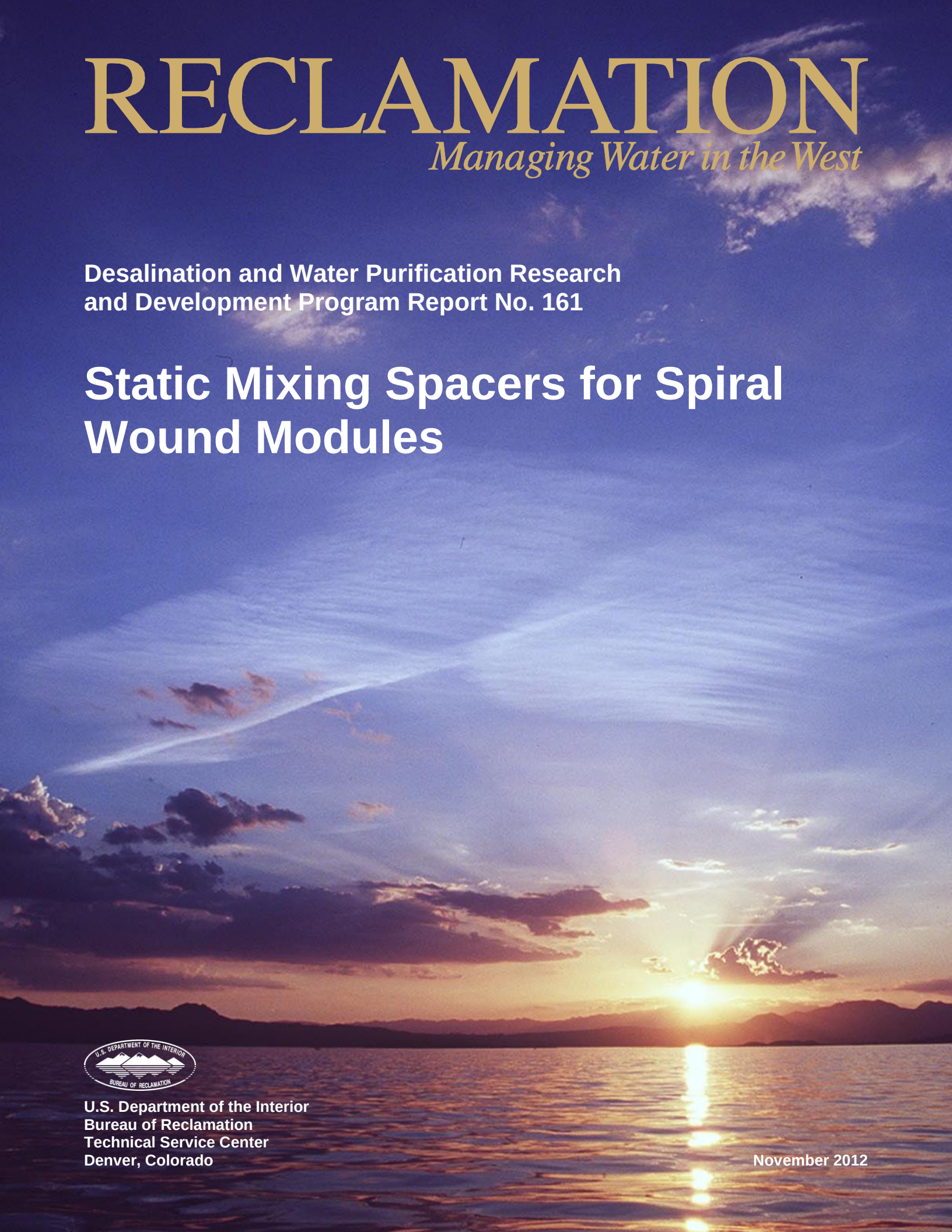

U.S. Department of the Interior
Bureau of Reclamation
Technical Service Center
Denver, Colorado

November 2012

REPORT DOCUMENTATION PAGE

Form Approved
OMB No. 0704-0188

1. REPORT DATE *(DD-MM-YYYY)*	2. REPORT TYPE	3. DATES COVERED *(From - To)*
November 2012	Final	2010-2012

4. TITLE AND SUBTITLE
Static Mixing Spacers for Spiral Wound Modules

5a. CONTRACT NUMBER
Agreement No.R10AP81213

5b. GRANT NUMBER

5c. PROGRAM ELEMENT NUMBER

6. AUTHOR(S)
Glenn Lipscomb

5d. PROJECT NUMBER

5e. TASK NUMBER

5f. WORK UNIT NUMBER

7. PERFORMING ORGANIZATION NAME(S) AND ADDRESS(ES)
Chemical Engineering
University of Toledo
3048 Nitschke Hall (MS 305)
1610 N Westwood Ave
Toledo, OH 43607
+1 419 530-8088
glenn.lipscomb@utoledo.edu

8. PERFORMING ORGANIZATION REPORT NUMBER
Task Identification Number
Task IV: Expanding Scientific Understanding of Desalination Processes
Subtask: Increase of rates of mass transfer to membrane or to heat transfer surfaces.

9. SPONSORING/MONITORING AGENCY NAME(S) AND ADDRESS(ES)
Bureau of Reclamation
U.S. Department of the Interior
Denver Federal Center
PO Box 25007, Denver, CO 80225-0007

10. SPONSOR/MONITOR'S ACRONYM(S)
Reclamation

11. SPONSOR/MONITOR'S REPORT NUMBER(S)
DWPR Report No. 161

12. DISTRIBUTION/AVAILABILITY STATEMENT
Online at https://www.usbr.gov/research/dwpr/DWPR_Reports.html

13. SUPPLEMENTARY NOTES

14. ABSTRACT
A novel static mixing spacer for planar flow channels has been evaluated experimentally and theoretically. The spacer moves fluid adjacent to the surfaces of the flow channel to the middle of the channel. Such mixing should help reduce concentration polarization and mitigate fouling due to precipitation or gelation of rejected species. The mixing is fundamentally different from that produced by conventional spacers that rely upon fluid vorticity or turbulence for mixing.

The results show fluid motion within the flow channel consistent with expectations. Flow visualization experiments using Computed Tomography further confirm the theoretical and experimental results.

15. SUBJECT TERMS
Desalination, static mixing spacer, ultrafiltration

16. SECURITY CLASSIFICATION OF:			17. LIMITATION OF ABSTRACT	18. NUMBER OF PAGES	19a. NAME OF RESPONSIBLE PERSON
a. REPORT	b. ABSTRACT	THIS PAGE			Yuliana Porras-Mendoza
U	U	U			19b. TELEPHONE NUMBER *(Include area code)* 303-445-2265

Standard Form 298 (Rev. 8/98)
Prescribed by ANSI Std. Z39.18

Mission Statements

The U.S. Department of the Interior protects America's natural resources and heritage, honors our cultures and tribal communities, and supplies the energy to power our future.

The mission of the Bureau of Reclamation is to manage, develop, and protect water and related resources in an environmentally and economically sound manner in the interest of the American public.

Disclaimer

The views, analysis, recommendations, and conclusions in this report are those of the authors and do not represent official or unofficial policies or opinions of the United States Government, and the United States takes no position with regard to any findings, conclusions, or recommendations made. As such, mention of trade names or commercial products does not constitute their endorsement by the United States Government.

Please note that this version of the report is directly from the original author.

Acknowledgments

[The Desalination and Water Purification Research and Development Program, Bureau of Reclamation is the sponsor of the research.

Table of Contents

List of Figures

List of Tables

Nomenclature

A	transport area (m^2)
B	one-half channel height (m)
c	concentration (kg/m^3)
d	length (m)
D	diffusion coefficient (m^2/s)
f	friction factor ($2\ d\ \Delta P/\rho/L/v^2$)
Gz	Graetz number ($Re\ Sc\ d/L$)
h	mass transfer coefficient (m/s)
H	channel height (m)
J	total mass transfer rate (kg/s) or water flux (m/s)
L	channel length (m)
L_p	hydraulic permeability (m/s/Pa)
P	wetted perimeter (m) or pressure (Pa)
Pn	Power number ($f\ Re^3$)
Re	Reynolds number (dv/ν)
S_{vsp}	spacer specific surface area (1/m)
Sc	Schmidt number (ν/D)
Sh	Sherwood number (hd/D)
v	velocity (m/s)

Greek

Δ	difference
ε	porosity
μ	viscosity (Pa s)
π	osmotic pressure (Pa)
ν	kinematic viscosity (μ/ρ, m^2/s)
ρ	density (kg/m^3)

Subscripts

atm	atmospheric value
b	bulk
c	characteristic or cross-sectional
Feed	feed value
h	hydraulic
in	inlet
lm	log mean
max	maximum value
n	normal
out	outlet
Retentate	retentate value
TM	trans-membrane
w	wall value

Executive Summary

A novel static mixing spacer for planar flow channels has been evaluated experimentally and theoretically. The spacer moves fluid adjacent to the surfaces of the flow channel to the middle of the channel. Such mixing should help reduce concentration polarization and mitigate fouling due to precipitation or gelation of rejected species. The mixing is fundamentally different from that produced by conventional spacers that rely upon fluid vorticity or turbulence for mixing.

Theoretical simulations of the spacer indicate significant enhancement in mass transfer coefficients is possible relative to an empty channel. The enhancement comes at the cost of increased pressure drop. However, for a given power input, the static mixing spacer can enhance mass transfer coefficients by a factor of three or more relative to an empty channel.

Samples of the spacer were fabricated using stereolithography. Spacer performance in terms of pressure drop and effective mass transfer coefficient was evaluated for the ultrafiltration of aqueous dextran solutions. The experimental results confirm the theoretical predictions: mass transfer coefficients were a factor of four higher for a given power input relative to an empty channel and more than a factor of two higher relative to a commercial spacer.

Additional measurements of pressure drop suggest flow through the test cell possesses an inertial component from fluid entry and exit into the cell that can be significantly larger than the viscous pressure drop through the spacer filled channel. A test cell would have to be constructed that allows pressure measurement along the length of the test cell to confirm this hypothesis.

Flow visualization experiments using Computed Tomography further confirm the theoretical and experimental results. The results show fluid motion within the flow channel consistent with expectations.

Introduction

Membrane separations have become a critical component of desalination and water treatment processes. Nanofiltration and reverse osmosis membranes often are used in the final purification step. These membranes typically are manufactured as flat sheets and provided for use in the form of a spiral wound module. The construction of a typical spiral wound reverse osmosis membrane module is illustrated in Figure 1.

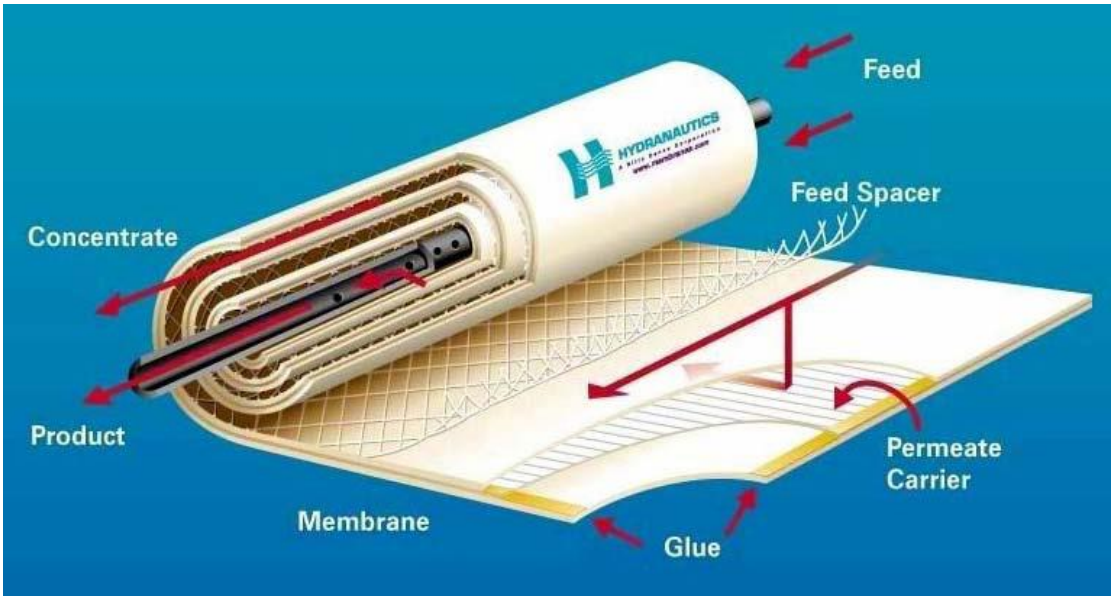

Figure 1. Illustration of typical spiral wound reverse osmosis membrane module [Bartels, et al., 2007].

The module consists of one or more membrane leaves or sandwiches that are wrapped around a central tube. Figure 1 illustrates a single leaf which consists of two membranes glued together separated by a permeate carrier; the membranes, carrier, and glue lines of the leaf are indicated in Figure 1. The permeate carrier creates a permeate collection space within the leaf through which the permeate (purified water product) can flow as illustrated by the red arrow *under* the upper membrane of the leaf in Figure 1. One end of the leaf is attached to the central tube in a fashion

that allows fluid communication between the permeate collection space and the interior of the central tube. The opposite end of the leaf is sealed by a glue line to force the collected permeate to flow towards the central tube from which the product is withdrawn.

The leaf is wrapped around the central tube to create a compact spiral wound module. Prior to wrapping, a feed spacer is placed on top of the leaf as illustrated in Figure 1. The feed spacer creates a space through which the feed can flow. As the feed flows parallel to the central tube along the width of the membrane leaf (indicated by the red arrow in Figure 1 *above* the upper membrane of the leaf) water permeates from the feed to the permeate collection channel. The module is placed within a case and the feed is introduced by contacting one end of the module with the feed solution so that it flows through openings created by the feed spacer. This design possesses a relatively high membrane surface area- to-volume ratio that minimizes the physical footprint of the process.

The permeate spacer must maintain an open space for the permeate flow given the trans-membrane pressure drop that exists in operation. For desalination, trans-membrane pressure drops can reach nearly 100 bar while low-energy modules may operate at pressures as low as 10 bar [http://www.dow.com/liquidseps/prod/filmtec.htm]. To withstand the trans-membrane pressure drop, a fine polyester mesh typically is used. The permeate spacer is designed to provide the required mechanical support while seeking to minimize the pressure drop required for permeate flow from the closed end of the leaf to the central permeate collection tube.

The feed spacer helps create uniform flow channels for the feed as the membrane leaf is wound around the central tube. Additionally, it can increase mass transfer rates by increasing shear rates within the feed channel and mixing the fluid in the direction normal to the membrane surface. This mass transfer rate increase arises from a reduction of the concentration of the

rejected species adjacent to the membrane surface. Reducing the surface concentration of rejected species also can reduce membrane fouling rates and thereby reduce the frequency of membrane cleaning. As with the permeate spacer, the increased pressure drop due to flow through the spacer must be considered simultaneously with mass transfer enhancement and fouling rates to determine an optimal design.

Commercially, most feed spacers are of a ladder or diamond design as illustrated in Figure 2.

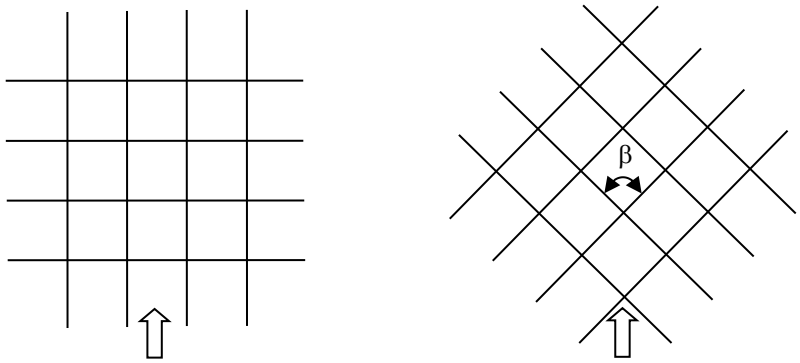

Figure 2. Ladder and diamond feed spacer designs. The primary feed flow direction is indicated by the arrow.

Design parameters for both types of spacers include: 1) filament diameter, 2) distance between filaments, and filament cross-sectional shape. The angle β is an additional parameter for the diamond design. Both types of can be woven from the individual filaments or layered as illustrated in Figure 3.

Figure 3. Woven and layered spacer cross-sections.

Literature Review

Enhancement of transport rates in channels through the introduction of flow obstacles such as spacers dates back to early studies of heat transfer in packed tubes [Colburn, 1931]. The first use of turbulence promoters in applications related to membrane processes appears to be in electrodialysis and filtration [Thomas et al., 1971; Leitz and Marinicic, 1977; Shen and Probstein, 1979; Schwager et al., 1980]. An explosion of work on experimental and theoretical evaluation of spacers in spiral wound modules has appeared in the literature since then.

Schwinge et al. [2004] provide an excellent review of the literature prior to 2004. Experimental measurements of mass transfer in spiral wound modules indicates the spacer can increase flux by a factor of 3-5 for fouling and non-fouling solutions [Light and Tran, 1981; Schock and Miquel, 1987; DaCosta et al., 1991; Polyakov and Karelin, 1992; DaCosta et al., 1993; Schwinge et al., 2000]. The mass transfer enhancement comes at the cost of increased pressure drop.

Computational fluid dynamics (CFD) has been used extensively to theoretically predict velocity and concentration fields in spiral wound modules and associated pressure drops and mass transfer rates. Early work [Cao et al, 2001; Karode and Kumar, 2001; Geraldes et al., 2002a, 2002b; Schwinge et al., 2002a, 2002b, 2003] focused on the velocity fields in two-dimensional cross-sections assumed to be representative of the three-dimensional spacer structure. The velocity fields were compared to experimental observations of mass transfer rates and membrane fouling. For example, CFD simulations predicted recirculation regions in front of and behind spacer filaments which correlated well with regions of reduced particle deposition during filtration [Schwinge et al., 2004]. The reduction in particulate deposition was attributed to

scouring of the membrane surface by the recirculation region. Subsequent work included explicit calculation of concentration fields and mass transfer rates [Wiley and Fletcher, 2002, 2003].

More recent work focuses on three dimensional simulations of flow through spacer filled channels [Li et al., 2002a, 2002b, 2004; Dendukuri et al., 2005; Ranade and Kumar 2006a, 2006b; Koutsou et al., 2007; Fimbres-Weihs and Wiley, 2007; Li and Tung, 2008]. This work commonly relies upon a periodic boundary cell to represent the spacer and membrane. Such periodic cells limit the mass transfer calculation to the well-developed mass transfer limit where the concentration field in a cross-section normal to the primary flow direction is independent of distance in the flow direction when scaled by the mixing cup average concentration [Leal, 2007]. The simulations are used to optimize spacer design based on predicted pressure drops and mass transfer rates.

Other work addresses transient flows through two-dimensional [Ahmad and Lau, 2006; Lau et al., 2010] and three-dimensional [Koutsou et al., 2009] spacer filled channels with simultaneous mass transfer across the membrane. For diamond spacers, the presence of an oscillating vortex in the primary flow direction and recirculation eddies near the filaments controls pressure drop and mass transfer.

Additional work addresses the effect of filament cross-sectional geometry on pressure drop and mass transfer [Guillen and Hoek, 2009] and simplified predictions of mass transfer rates [Shrivastava et al., 2008]. For the nanofiltration and reverse osmosis operating conditions considered, Guillen and Hoek conclude the filament geometry influences pressure drop more than product water quality. However, for moderate Reynolds numbers, some variation in Sherwood number (dimensionless mass transfer coefficient) is evident. Shrivastava and co-workers conclude the Leveque solution [Leal, 2007] for entry mass transfer may be used to

estimate the average mass transfer coefficient for a ladder-type spacer filled channel. They use the Leveque solution to evaluate the local mass transfer coefficient based on the local channel height and average the local values over the length of the flow channel. Predicted Sherwood numbers are in good agreement with experiment and CFD calculations but the basis for this agreement is not understood.

The available literature on feed spacer design comprehensively explores experimental and theoretical evaluation of spacer geometry on momentum and mass transfer in spiral wound modules. However, this literature focuses primarily on the ladder and diamond designs illustrated in Figure 2. Notable exceptions include the use of multi-layer spacers consisting of a stack of three or more ladder or diamond spacers [Li et al., 2005; Balster et al., 2006; Fimbres-Weihs and Wiley, 2008] or the use of twisted tapes alone or in a stacked configuration with a ladder or diamond spacer [Li et al., 2005]. Integrating the spacer with the membrane also has been proposed [Balster et al., 2010].

Despite this activity, spacers with lower pressure drops and higher mass transfer coefficients are desired to reduce water treatment costs. Such improved spacers could be used in the nanofiltration, reverse osmosis, and ultrafiltration spiral wound modules used in the process.

The reported work is a theoretical and experimental study of a new paradigm for feed spacer design. The design is equivalent to a static mixer for planar flow channels and provides mixing to reduce concentration polarization and increase mass transfer rates without the generation of vorticity or eddies. The spacer moves fluid adjacent to the membrane surface to the center of the flow channel and vice versa thereby reducing the surface concentration of rejected species, increasing mass transfer rates, and potentially reducing fouling.

Static Mixing Spacer Design

A prospective view of the proposed static mixing spacer design is provided in Figure 4. Fluid flow is in the z direction and the contacting membranes lie above and below the section shown in the y-z plane. The entire spacer is created from the portion shown by replicating the section and translating it along the y axis to create a strip that spans the flow channel width as shown in Figure 5. Multiple strips are connected by filaments to form a spacer sheet. Note that the spacing between strips is a design parameter as well as the dimensions of the section in Figure 4. Top and bottom views of the section in Figure 4 are shown in Figure 6. The cross-sections A-A' and B-B' in Figure 6.are illustrated in Figure 7.

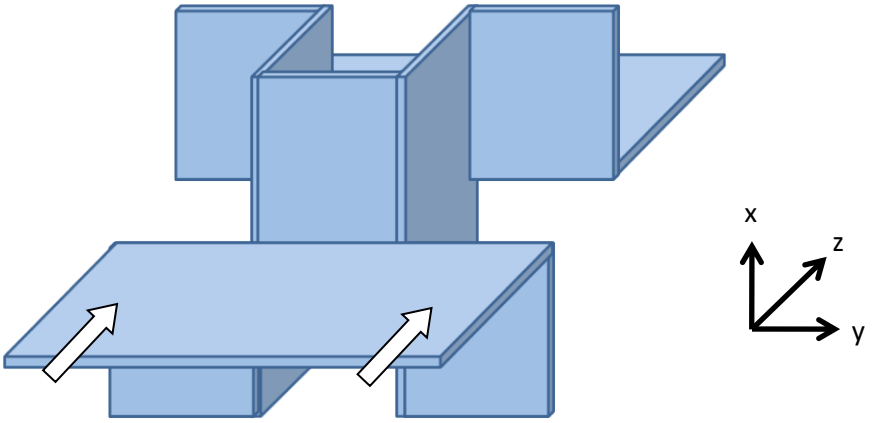

Figure 4. Perspective view of proposed static mixing spacer design. Fluid flow is in the z direction. The section shown is reproduced and translated in the y direction to span the width of the flow channel. The contacting membranes lie in the y-z plane above and below the spacer. Feed flow is indicated by the white arrows.

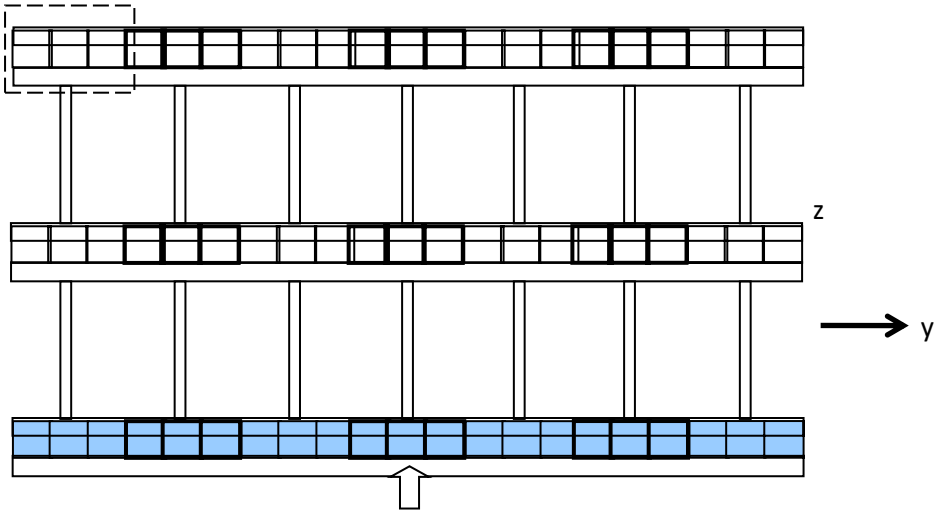

Figure 5. Illustration of a partial spacer sheet created by replicating and translating the section shown in Figure 4. The dashed box encloses one copy of the section which is replicated and translated along the y axis to create a strip. Multiple strips are held together by filaments to create a spacer sheet. The arrow indicates the feed flow direction.

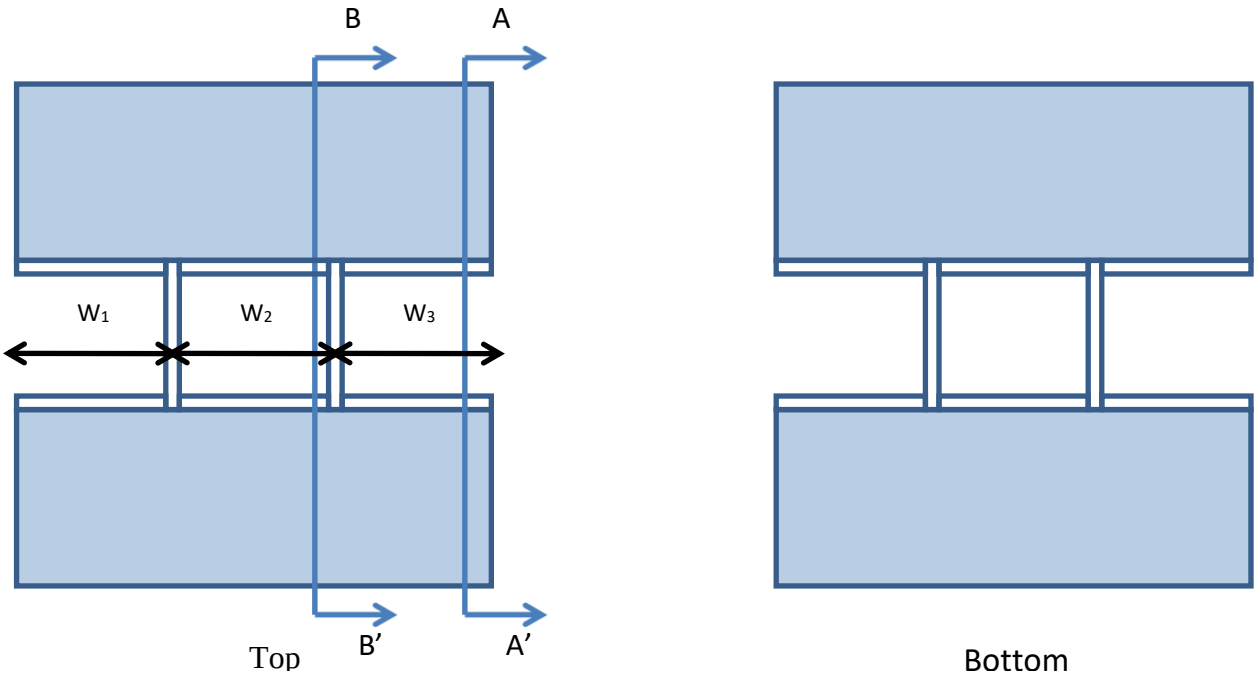

Figure 6. Top and bottom views of the section shown in Figure 4. Design dimensions are indicated. The darker blue regions indicate where the spacer contacts the membranes that lie above and below the section.

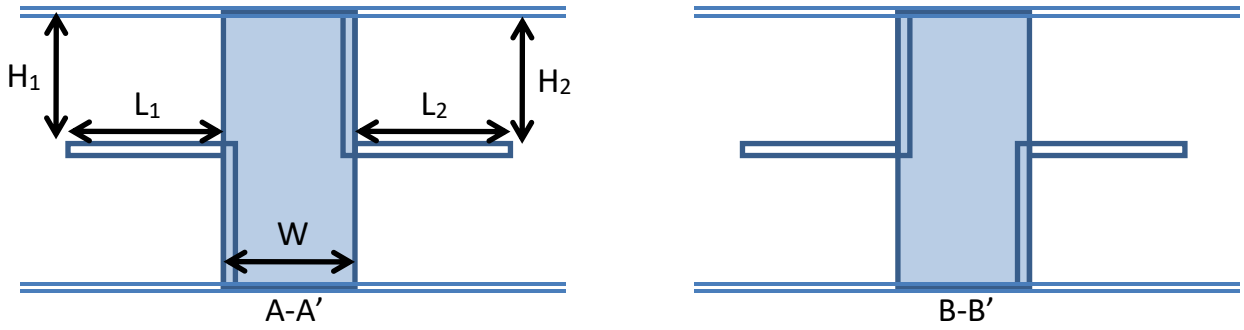

Figure 7. Cross-section A-A' and B-B' of Figure 6. Design dimensions are indicated. The double lines above and below the section represent the membrane.

The operation of the proposed spacer is illustrated schematically in Figure 8. The feed flows from bottom to top in the figure between two membranes as would occur between the leaves of a spiral wound module. The semi-permeable membranes allow transport of the feed solvent but selectively reject dissolved solutes.

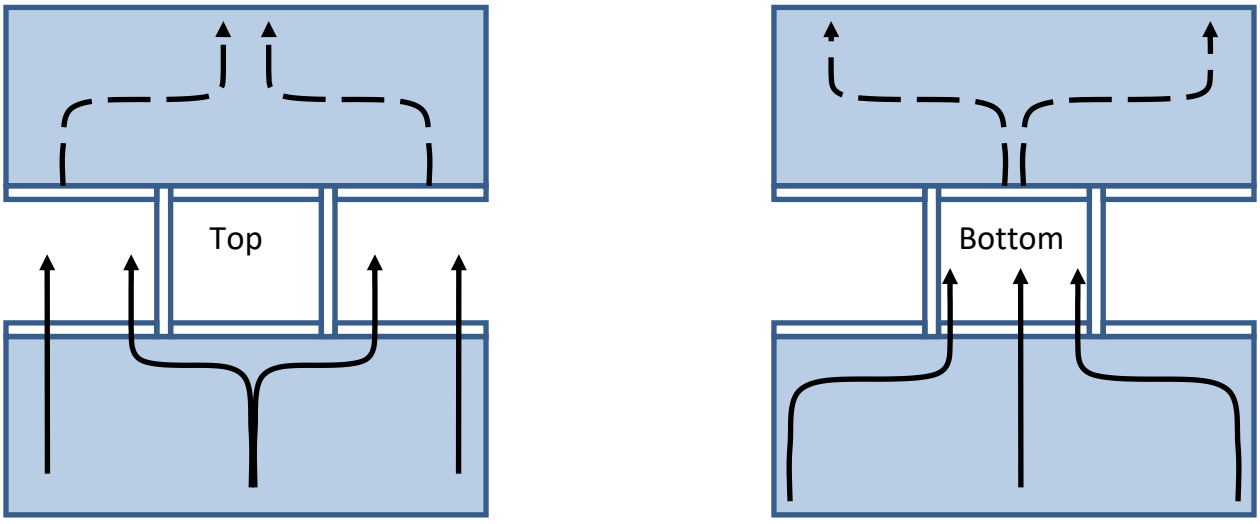

Figure 8. Top and bottom view of the fluid streamlines through the section illustrated in Figure 4. Note the leading and trailing edges of the section divide the flow in two. For the top view, solid lines indicate streamlines are visible from the top and dashed lines indicate streamlines are not visible. For the bottom view, solid lines indicate streamlines are visible from the bottom and dashed lines indicate streamlines are not visible.

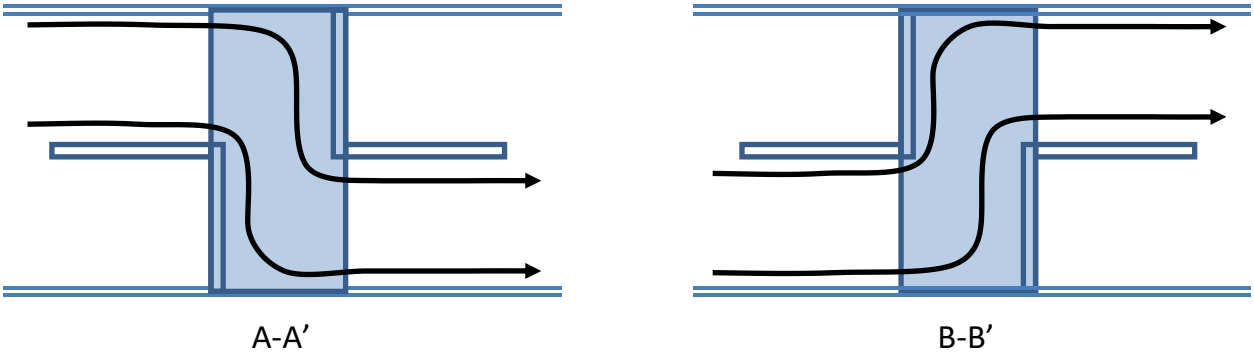

Figure 9. Streamlines in sections A-A’ and B-B’. Flow is from left to right.

In the top view, the feed flows from the top through the chimneys or openings in the spacer to the bottom and vice versa in the bottom view. The streamlines in sections A-A’ and B-B’ are illustrated in Figure 9. In section A-A’, the streamline adjacent to the top membrane in Figure 9 moves to the center of the flow channel while the streamline in the center of the flow channel moves adjacent to the membrane surface. Similar behavior is apparent in the bottom view and section B-B’. Figures 8 and 9 illustrate the ability of the proposed spacer to move fluid adjacent to the membrane surface to the center of the flow channel, and vice versa, without the generation of vorticity or eddies. This movement brings the fluid containing a higher concentration of the rejected solute to the center of the flow channel where diffusion can reduce the concentration. Moreover, fluid is brought to the membrane with a lower solute concentration. This disruption of growth in the concentration boundary should significantly enhance mass transfer rates.

Simulation of Spacer Performance

Simulations were performed of flow and transport in spacer filled channels using ANSYS Fluent and COMSOL Multiphysics ®. Both are commercial computational fluid dynamics (CFD) packages that solve the governing conservation equations by meshing (i.e., discretizing) the

solution domain and converting the partial differential conservation equations into sets of non-linear algebraic equations. The algebraic equations are solved using an iterative numerical procedure to obtain values of the field variables (velocity, pressure, and concentration) at specific points in the solution domain. The point values are used to determine overall pressure drop and transport rates.

Creation of Solution Domain

SolidWorks (Dassault Systèmes SolidWorks Corp.) is used to create a scale model of spacer elements. SolidWorks creates a 3D solid geometry in a part or assembly document. The document can be used to create drawings for photo-realistic visualization and manufacturing.

The model is created by drawing a 2D projection of a section of the spacer and extruding it to form a 3D section. Multiple sections can be combined by addition or subtraction to produce complex features of the object.

A typical spacer element model is shown in Figure 10. The element was created by adding and subtracting sections produced by extruding portions of the 2D projection of the spacer element illustrated in Figure 11. Figure 11 also indicates the key design dimensions of the element. Note that the thickness of the solid regions, dimension D, is the same throughout the element. Variations in thickness could be taken as an additional design variable but was considered outside the scope of the present work.

SolidWorks can export models in a wide range of formats including 3D XML, IGES, and Parasolid for import into other programs. Fluent and COMSOL (with the CAD Import Module) are able to read Parasolid file formats for creating complex solution domains.

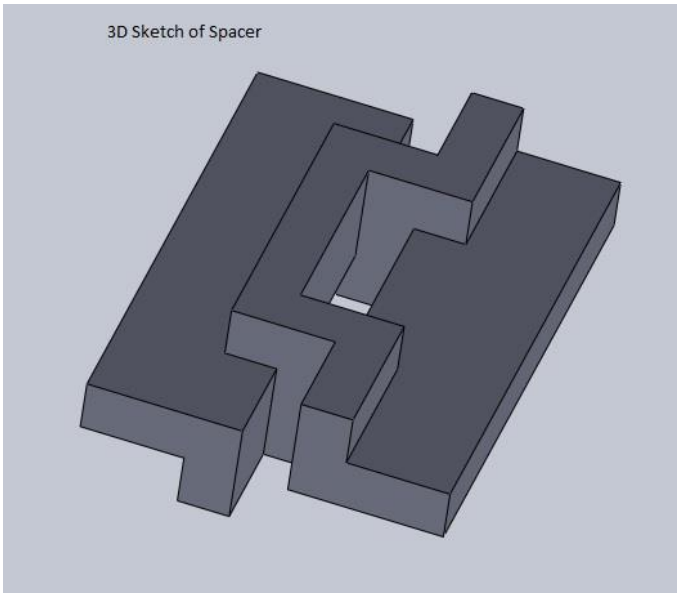

Figure 10. Typical SolidWorks model of a spacer element.

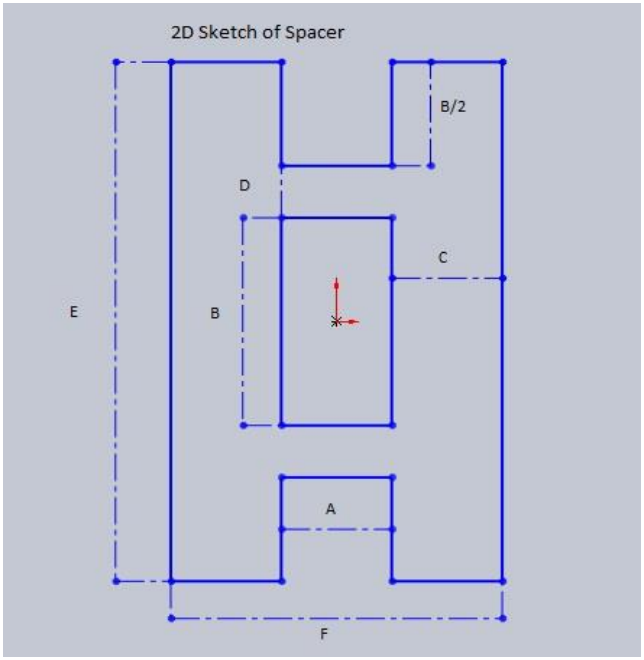

Figure 11. 2D projection of spacer element with design dimensions.

After importing the 3D spacer model into Fluent or COMSOL, the solution domain is created by subtracting the solid spacer model from a solid rectangular slab possessing the

dimensions of the flow channel; solid rectangular slabs can be generated readily within Fluent or COMSOL for this purpose. A typical solution domain is illustrated in Figure 12. Additional dimensions used to define the solution domain are indicated in Figure 12.

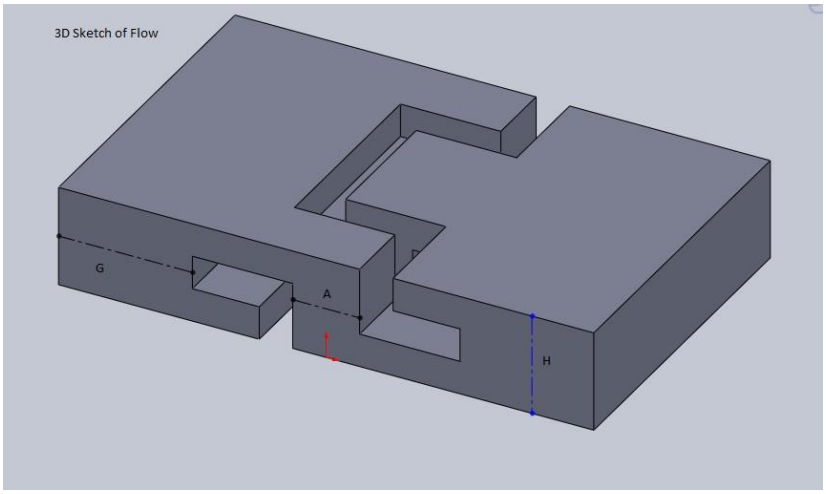

Figure 12. Typical solution domain used in the simulations.

The solution domain is discretized or meshed within the Fluent and COMSOL environments using the mesh generation tools provided. Automatic mesh generation is possible in both environments with control of refinement level. The level of refinement impacts the solution quality. Higher levels of refinement provide more accurate solutions but at the expense of longer simulation times. Although a rigorous estimate of the error associated with discretization of the solution domain (and the algorithm used to convert the governing partial differential equations to algebraic equations with CFD) cannot be provided, the effect of refinement level on key simulation results typically is reported to determine the accuracy associated with a given level of refinement.

Within COMSOL, only automatic mesh generation was used. Within Fluent, manual meshing was used primarily to create structured meshes with hexahedron elements that possess

greater solution accuracy due to the type and degree of interpolation within the element and the ability to control element aspect ratio (skewness or quality) relative to the unstructured meshes created with tetrahedron elements with automatic meshing. Higher quality meshes are desirable especially along the membrane surface where large concentration gradients can exist in the entry mass transfer limit. Moreover, structured meshes allow the use of higher order solvers that reduce the computational time required to obtain a solution.

To create a structured mesh, the domain is divided into a number of subregions as illustrated in Figure 13. The number of nodes is specified along the edges of the subregions and these nodes are used to create the fully meshed solution domain as illustrated in Figure 14. The mesh can be refined by increasing the number of nodes along an edge or using a boundary adaption algorithm.

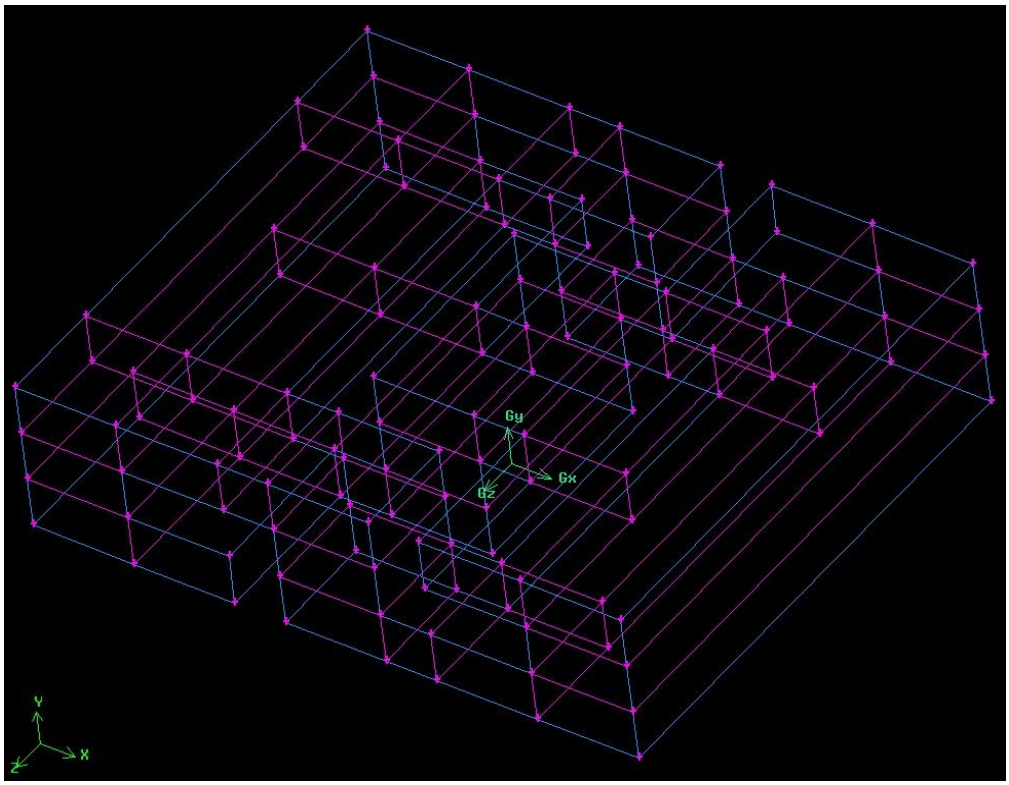

Figure 13. Typical subdivided flow domain used for meshing.

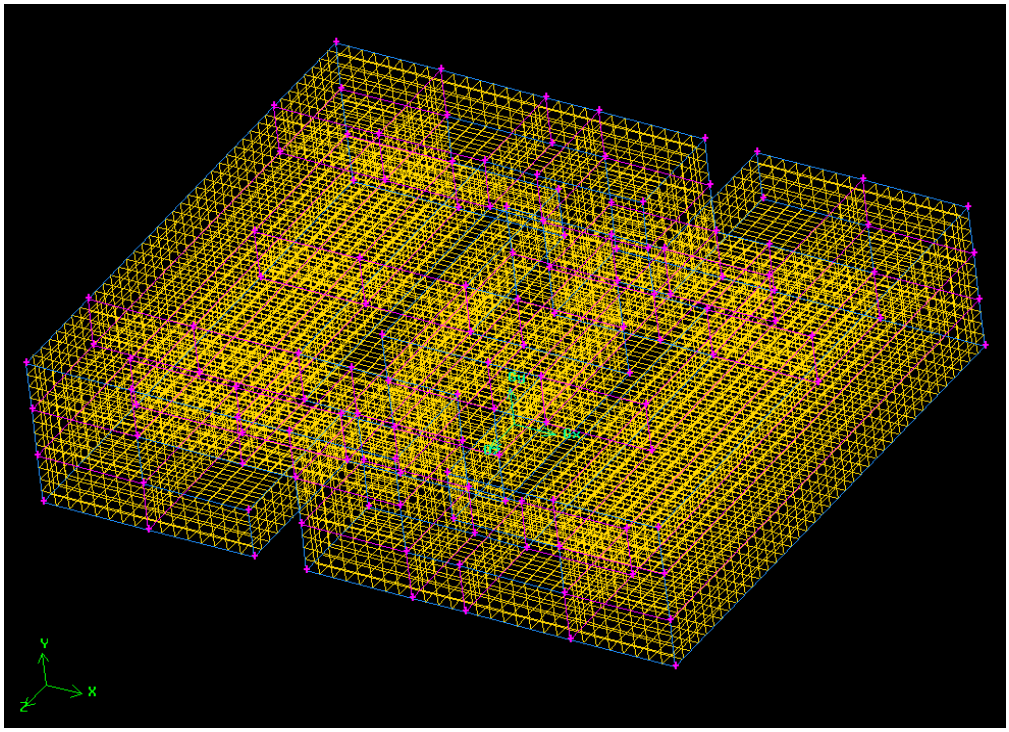

Figure 14. Typical final meshed solution domain.

Simulation Boundary Conditions.

Two types of simulations were performed. In the first, selectively permeable membranes bounded the top and bottom of the solution domain illustrated in Figure 14. In the second, the top was bounded by a membrane and the bottom by an impermeable, stationary wall.

Appropriate boundary conditions for solution of the conservation of momentum equations for both simulations are:

1. membrane and spacer boundaries: no-slip, zero velocity boundary condition
2. inlet boundary: specified bulk velocity
3. outlet boundary: pressure outlet with zero gauge pressure at one node on boundary
4. left and right side boundaries: symmetry

Boundary conditions for solution of the species conservation of mass equation are:

1. membrane boundaries: constant concentration
2. spacer boundaries: zero normal mass flux
3. inlet boundary: constant concentration
4. outlet boundary: convective mass transfer (negligible concentration gradients along flow direction)
5. left and right side boundaries: symmetry

The boundary conditions used for the solution of the species conservation of mass equation are for transport of a dilute *solute* to the membrane surface – not for *solvent* transport across the membrane. This simplifies the solution in that the velocity field is unaffected by mass transfer (loss or gain of a dilute solute will not lead to significant changes in the mass flow rate and associated velocity fields) and reduces simulation times. The literature indicates that mass transfer results obtained assuming an impermeable wall differ by less than 25% from results obtained with wall permeation [Miranda and Campos, 2002]. The differences appear to be negligible when the ratio of the osmotic pressure to trans-membrane pressure is greater than 0.8. If the ratio is less than 0.8, the use of a uniform solute transport rate to the membrane surface appears to give equivalent mass transfer results.

This type of mass transfer problem is computationally identical to the analogous heat transfer problem for incompressible fluids. The governing conservation of mass and energy equations are identical upon defining a thermal diffusivity for the heat transfer problem which is equal to the ratio of the thermal conductivity to the product of the density and heat capacity, $D_T = k/(\rho C_p)$ and neglecting energy generation by viscous heating or other sources. Hence, the heat transfer problem can be solved to obtain the heat transfer coefficient which is numerically equal

to the equivalent mass transfer coefficient. The calculation of heat fluxes is more facile in Fluent since it does not require the creation of custom user defined functions (UDFs) for calculating transport rates along surfaces of the solution domain.

Liquid water was used as the fluid with specific properties tabulated in Table 1.

Property	Liquid (water)
Density [kg/m^3]	1015
Viscosity [kg/m/s]	0.00215
Thermal Conductivity [W/m/k]	0.600

Table 1: Fluid properties used in the simulation.

Discretization and Solution of the Conservation Equations

COMSOL transforms the governing partial differential conservation equations into a set of non-linear algebraic equations using the finite element algorithm. The finite element method relies upon dividing the solution domain into a set of sub-volumes or elements within which an algebraic variation of the field variables is assumed; this division is the meshing step discussed previously. The algebraic equations are obtained by substituting the assumed algebraic form for the field variables into the governing equations and integrating the equations with respect to a weighting function. In the weak formulation, the weighting function is taken to be the same as the assumed algebraic variation of the field variables. This set of equations is solved using one of a set of non-linear solvers; commonly an affine invariant form of the damped Newton method is used. Each iteration of this method requires solution of a set of linear equations which may be solved using a direct or iterative solver as provided by COMSOL.

Fluent transforms the governing partial differential conversation equations into a set of non-linear algebraic equations using the finite volume algorithm. Like the finite element, the

solution domain is divided into a set of sub-volumes or elements. However, the finite volume method does not prescribe a variation of the field variables within each element. Instead, a single value is assigned to the point at the center. Integration of the conversation equations over each element yields a set of equations that require specification of fluxes across the faces of each element and values of the field variables at the center of each face.

Convective fluxes were calculated using the least square cell-based algorithm and the values at the center of the faces using second-order upwind finite differencing. Additionally, momentum weighted averaging and the SIMPLE-Consistent algorithm for coupled pressure-velocity corrections were used for the continuity equation to enhance the pressure calculation. The PRESTO (Pressure Staggering Option) scheme was used for pressure interpolation.

To start the iterative solution procedure, an initial guess for the solution is required. Commonly, the initial guess is for a uniform flow with constant pressure and concentration/temperature in which the velocity, pressure, and concentration/temperature are all set equal to the values at the inlet. Alternatively, the pressure and concentration may be set equal to the inlet values and the velocity field to zero except along the inlet boundary.

The solution for the concentration field (or temperature field where the conservation of mass and energy equations are identical) is used to evaluate transport to the membrane surface. Both COMSOL and Fluent offer capabilities to calculate flux across a surface from the solution for the velocity, concentration, and temperature fields.

The total rate is converted to an average mass (or heat) transfer coefficient by dividing by the area available for transport and by the log-mean concentration (or temperature) difference:

$$h = \frac{J}{A\Delta c_{lm}} \tag{1}$$

To calculate the log-mean difference, the bulk fluid value is calculated by integrating the product

of velocity and concentration (or temperature) along the inlet and outlet planes and dividing by the total volumetric flow rate:

$$c_b = \frac{\int_{in\ or\ out} v_n c dA}{\int_{in\ or\ out} v_n dA} \tag{2}$$

where v_n is the normal velocity to the inlet or outlet plane and the integral extends over the area A of the inlet (subscript in) or outlet (subscript out) plane. For a fixed concentration (or temperature) at the membrane surface, the log-mean value is calculated from the difference between the surface value and the bulk fluid concentration:

$$\Delta c_{lm} = \frac{\Delta c_{out} - \Delta c_{in}}{\ln\left(\frac{\Delta c_{out}}{\Delta c_{in}}\right)} \tag{3}$$

where Δ indicates the difference between the bulk and surface values.

The average mass (or heat) transfer coefficient is non-dimensionalized using the diffusivity (or thermal diffusivity) to obtain the Sherwood number (Sh):

$$Sh = \frac{h d_h}{D} \tag{4}$$

where D is diffusivity and d_h a characteristic length of the flow channel. In previous work, several different geometrical parameters have been used as the characteristic length including: 1) channel height, 2) filament thickness (or other spacer characteristic dimension), and 3) hydraulic diameter. Equation (5) may be used to calculate the hydraulic diameter for two dimensional, unobstructed flow channels:

$$d_h = \frac{4A_c}{P} \tag{5}$$

where A_c is the cross-sectional area of the flow channel and P the wetted perimeter. However, for spacer filled channels, A_c varies with distance along the flow channel which confounds its

computation and Equation (6) often is used instead:

$$d_h = \frac{4\epsilon}{(2/H) + (1-\epsilon)S_{vsp}} \tag{6}$$

where ε is the porosity of the spacer filled channel, H the channel height, and S_{vsp} the specific surface of the spacer. The channel height is used here as the characteristic dimension because it leads to the same value for Reynolds number for a given channel height and feed flow rate for each spacer; if the hydraulic diameter is used, the Reynolds number is a function of spacer geometry as well. This facilitates comparing the performance of spacers in a given channel for a given flow rate.

Past analyses of convective mass transfer suggest the Sherwood number dependence on the Reynolds (*Re*) and Schmidt (*Sc*) number should be given by Equation (7):

$$Sh = \frac{hd_c}{D} = \alpha\left(\frac{d_c v_b}{\nu}\right)^a \left(\frac{\nu}{D}\right)^b \left(\frac{d_c}{L}\right)^c = \alpha Re^a Sc^b \left(\frac{d_c}{L}\right)^c \tag{7}$$

where v_b is the bulk fluid velocity, ν the kinematic viscosity, and L the flow channel length. The constants α, a, b, and c are geometry dependent. For entry mass transfer (i.e., sufficiently high flow rates that the mass transfer boundary layer is much smaller than the channel height), analytical solutions for empty channels further suggest the Sherwood number should be proportional to the Graetz number raised to the one-third power where the Graetz number is defined by Equation (8):

$$Gz = Re\ Sc\left(\frac{d_c}{L}\right) \tag{8}$$

which follows from Equation (7) by setting a=b=c=1/3. Additionally, the analytical results suggest the Sherwood number approaches a constant value in the well-developed mass transfer limit (i.e., sufficiently low flow rates that the mass transfer boundary layer extends across the flow channel). Based on these observations, simulation results are presented as the dependence

of Sherwood number on Graetz number or Sherwood number scaled by the product of Schmidt number and d_c/L on Reynolds number.

The calculated pressure drop is non-dimensionalized by calculating the friction factor defined by Equation (9):

$$f = \frac{2d_c \Delta \mathrm{P}}{\rho L v_b^2} \tag{9}$$

The literature suggests the friction factor should be a function of Reynolds numbers as given by Equation (10):

$$f = \beta Re^e \tag{10}$$

where β and e are geometry dependent. Consequently, simulation results are presented as the dependence of friction factor on Reynolds number.

Spacers increase mass transfer coefficients at the expense of increased pressure drop. To compensate for this effect when comparing spacers, the literature suggests plotting the Sherwood number versus the Power number defined by Equation (11):

$$Pn = fRe^3 \tag{11}$$

The Power number is the dimensionless value of the product of bulk velocity and pressure drop and is a measure of the power required to pump the fluid through the feed channel. For a given power input, spacer designs that maximize mass transfer rates (i.e. value of the Sherwood number) are most desirable since required membrane area is minimized. However, the economic optimum spacer design will depend on the relative costs of membrane, spacer, and power.

Simulation Validation

To help establish the validity of a numerical simulation procedure, simulations often are performed for a case for which an analytical solution is available or the literature contains results from previous studies. The simulation of transport in a membrane bounded rectangular channel without a spacer is used here to establish simulation validity.

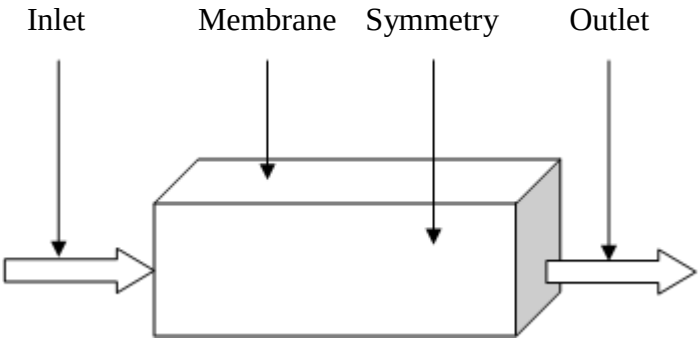

Figure 15. Empty channel solution domain and boundary conditions.

Figure15 illustrates the solution domain. The front and back surfaces of the channel are symmetric so the force acting on the surfaces and the normal mass fluxes (or thermal fluxes for the equivalent heat transfer problem) are zero. Boundary conditions for the other surfaces are:

1. uniform velocity and concentration (or temperature) along the inlet
2. no-slip and uniform wall concentration (or temperature) along the upper and lower bounding surfaces
3. zero force in the normal direction and convective species mass transfer (or heat transfer) along the outlet

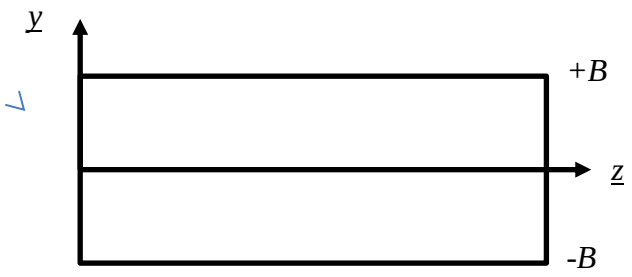

Figure 16. Two-dimensional solution domain for mass transfer of a dilute solute in an infinite slit. The top and bottom boundaries lie at *y*=+/- *B*.

For transport of a dilute species, the velocity field will be unaffected by mass transfer and identical to that for flow in an infinite slit – a parabolic velocity profile that depends only on the normal distance from the channel walls. Moreover, the three-dimensional species mass transfer problem can be reduced to a two dimensional problem in the solution domain illustrated in Figure 16.

The two-dimensional can be solved analytically in two mass transfer limits [Iranshahi, 2012]: 1) entry and 2) well-developed. In the entry limit, flow rates are high enough and mass transfer rates low enough that a thin concentration boundary layer forms along the channel surfaces. A similarity transform yields an analytical solution for the concentration field. This solution provides the following expression for the Sherwood number:

$$Sh = \frac{hB}{D} = 1.28\alpha \left(\frac{B v_{max}}{\nu}\right)^{1/3} \left(\frac{\nu}{D}\right)^{1/3} \left(\frac{B}{2L}\right)^{1/3} = 1.28 Gz^{1/3} \tag{12}$$

where the Graetz number for the slit flow is defined in Equation (12).

In the well-developed limit, the eigenfunction expansion of the solution for the concentration field is dominated by the eigenfunction associated with the smallest eigenvalue. Solving for the smallest eigenvalue and associated eigenfunction yields the solution for the concentration field and the following expression for the Sherwood number:

$$Sh = \frac{hB}{D} = 3.77 \tag{13}$$

Simulation results obtained for transport in the solution domain of Figure 15 are compared to the analytical solutions in the entry and well-developed limits in Figure 17. A mesh refinement study indicated the simulation results are accurate to less than 2%. Good agreement exists between the two solutions providing support for the validity of the simulation procedure.

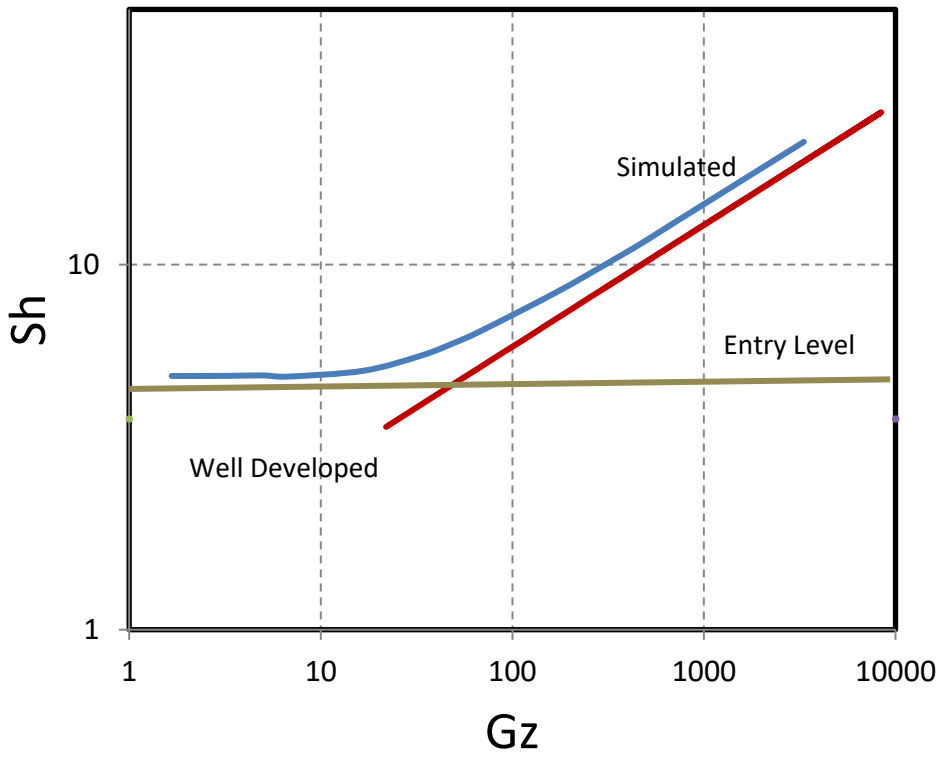

Figure 17. Comparison of simulation results to analytical solutions for mass transfer in an infinite slit.

Simulation Results

A preliminary evaluation of spacer design dimensions was performed for spacers possessing the range of dimensions in Table 2. The design dimensions are illustrated in Figures 11 and 12.

A	*B*	*C*	*D*	*E*	*F*	*G*	*H*
1-2	4-8	1-2	1	10-18	6-8	2-8	3

Table 2.Ranges of design dimensions considered. All values are in mm.

The preliminary evaluations were performed for spacers placed in a flow channel or slit of height *H*, width *E*, and length *F*+2*G* (i.e., the flow channel extends a distance *G* before and after the leading and trailing edges of the spacer, respectively) with membranes above *and* below the spacer.

The dimensions of the spacers simulated are provided in Table 3 as well as the values of α, *a*, β, and *e* obtained from the results. Note that the values for α and *a* in Equation (7) were obtained from results for the highest Graetz numbers (i.e., the entry mass transfer limit) where a log-log plot yielded a linear relationship between *Sh* and *Gz*; the constants *b* and *c* were assumed to be equal to *a* as expected in the entry mass transfer limit.

Spacer	A	B	C	D	E	F	G	H	α	*a*	β	*e*
1	1	4	2	1	10	7	2	3	2.14	0.321	194	-0.988
2	2	4	2	1	10	8	2	3	2.25	0.320	267	-0.988
3	2	8	2	1	18	8	2	3	1.96	0.328	181	-0.991
4	2	4	1	1	10	6	2	3	1.90	0.326	190	-0.986
5	2	4	2	1	10	8	4	3	2.16	0.314	171	-0.989
6	2	4	2	1	10	8	8	3	2.08	0.316	140	-0.987
7	2	8	2	1	18	8	4	3	1.86	0.332	157	-0.988
8	2	8	2	1	18	8	8	3	1.82	0.332	130	-0.991
Slit									1.52	0.333	24	-1.000

Table 3. Dimensions (mm) of spacers simulated and simulation values for α, *a*, β, and *e*.

The values for the slit are in excellent agreement with analytical solutions. The results indicate that spacer 2 gives the highest mass transfer coefficient in the entry mass transfer limit but also possesses the highest pressure drop. Spacer 8 gives the lowest mass transfer coefficient and

pressure drop. All spacers give higher mass transfer coefficients than an empty channel or slit.

Figure 18 compares the simulation results for spacers 2 and 8 (which were selected for further study) as well as an empty slit for a broad range of Graetz numbers that extends beyond the entry mass transfer limit. The results indicate the spacers give higher mass transfer coefficients from the entry to the well-developed mass transfer limits.

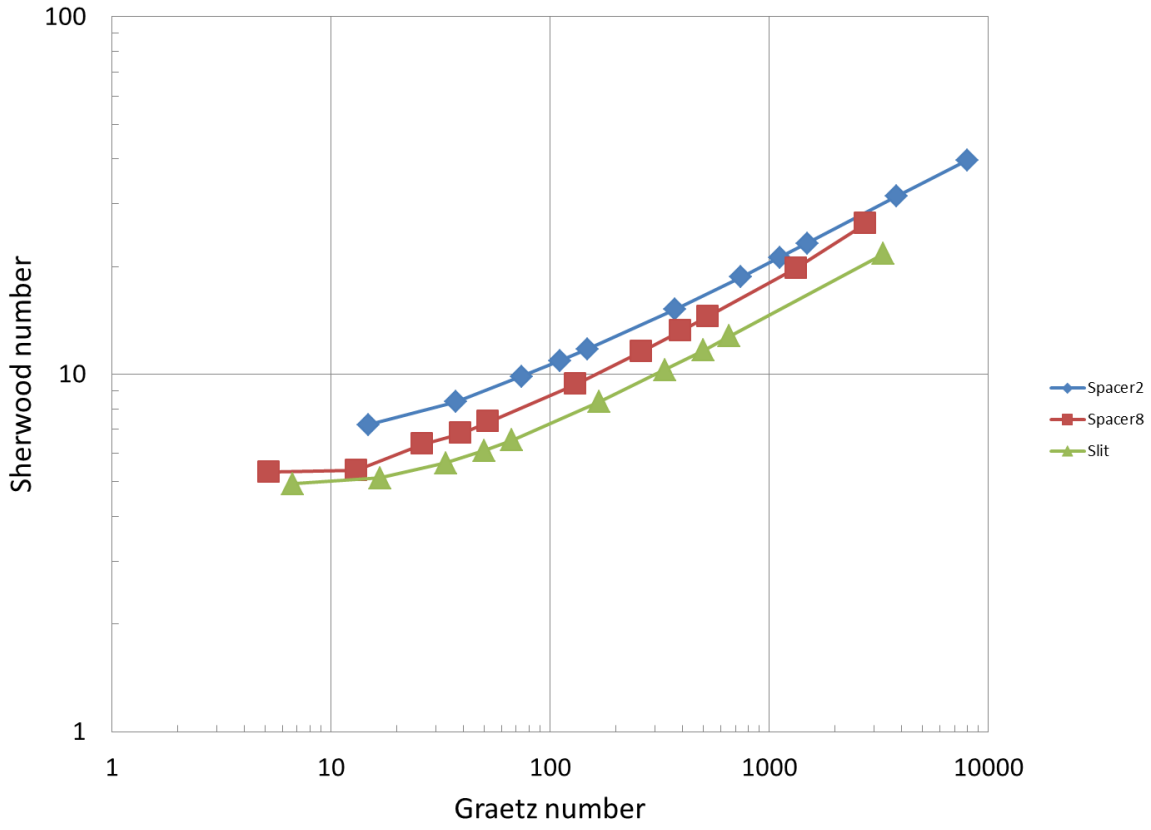

Figure 18. Sherwood number dependence on Graetz number for spacers 2 and 8 as well as an empty slit.

The friction factor dependence on Reynolds number is illustrated in Figure 19. For the Reynolds number range considered, the friction factor is inversely proportional to Reynolds number as expected for laminar flow. Additionally, pressure drops through spacer filled channels can be up to an order of magnitude greater than the pressure drop through an empty channel.

The Sherwood number dependence on Power number is illustrated in Figure 20. The Sherwood number is scaled by the product of Schmidt number and channel height-to-length ratio raised to the one-third power to yield a value that is dependent only on Reynolds number in the entry mass transfer limit based on the results presented in Table 3. Therefore, the curves in Figure 20 are dependent only on the Reynolds number.

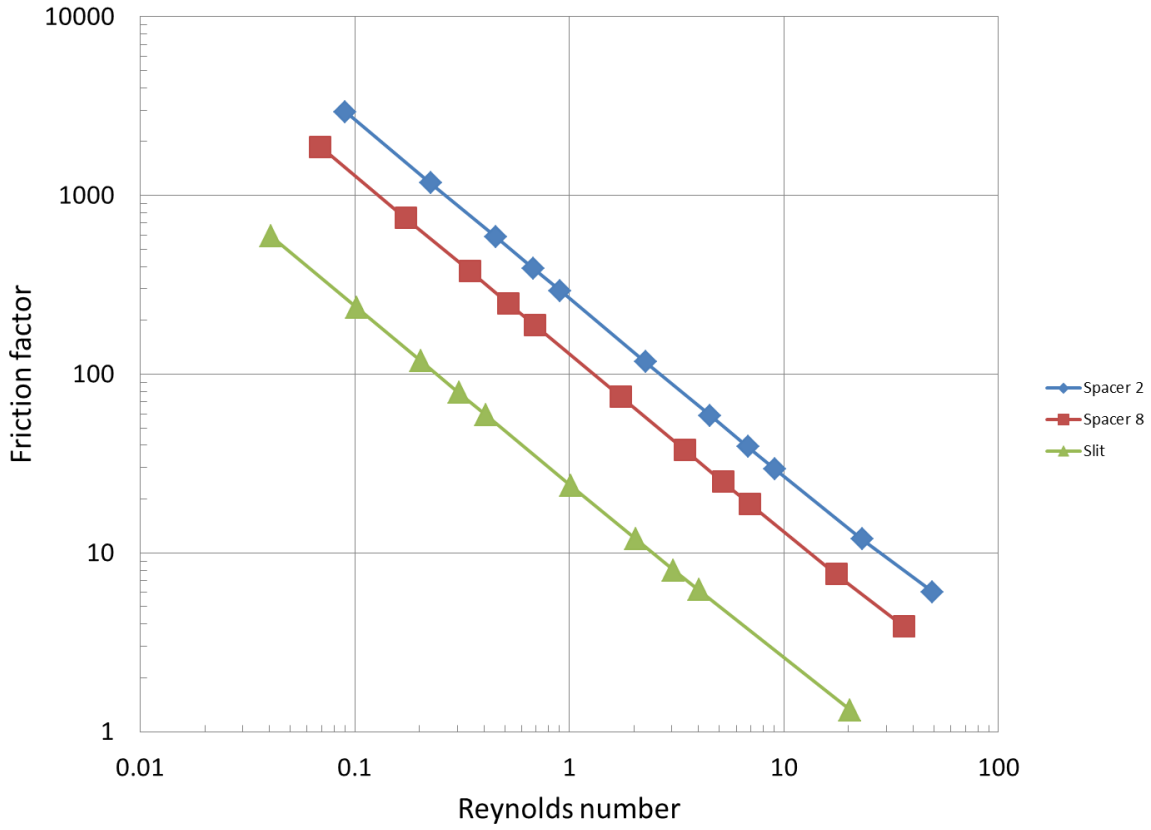

Figure 19. Friction factor dependence on Reynolds number for spacers 2 and 8 as well as an empty slit.

Figure 20 indicates the spacers and slit give comparable performance in the entry mass transfer region (i.e., high Reynolds or Power number) since for a given power input mass transfer coefficients are nearly identical. However, as the transition to the well-developed mass transfer limit occurs, the spacers give better performance.

The lack of improvement in spacer performance in the entry limit is due to the length of the flow channels considered. Simulations were limited to flow channels that contained only a single spacer element and the results were compared to empty channels of approximately one-half the length. If unobstructed flow channel lengths are nearly identical, the boundary layers that develop will be of comparable thickness which is the case for the results in Figure 20.

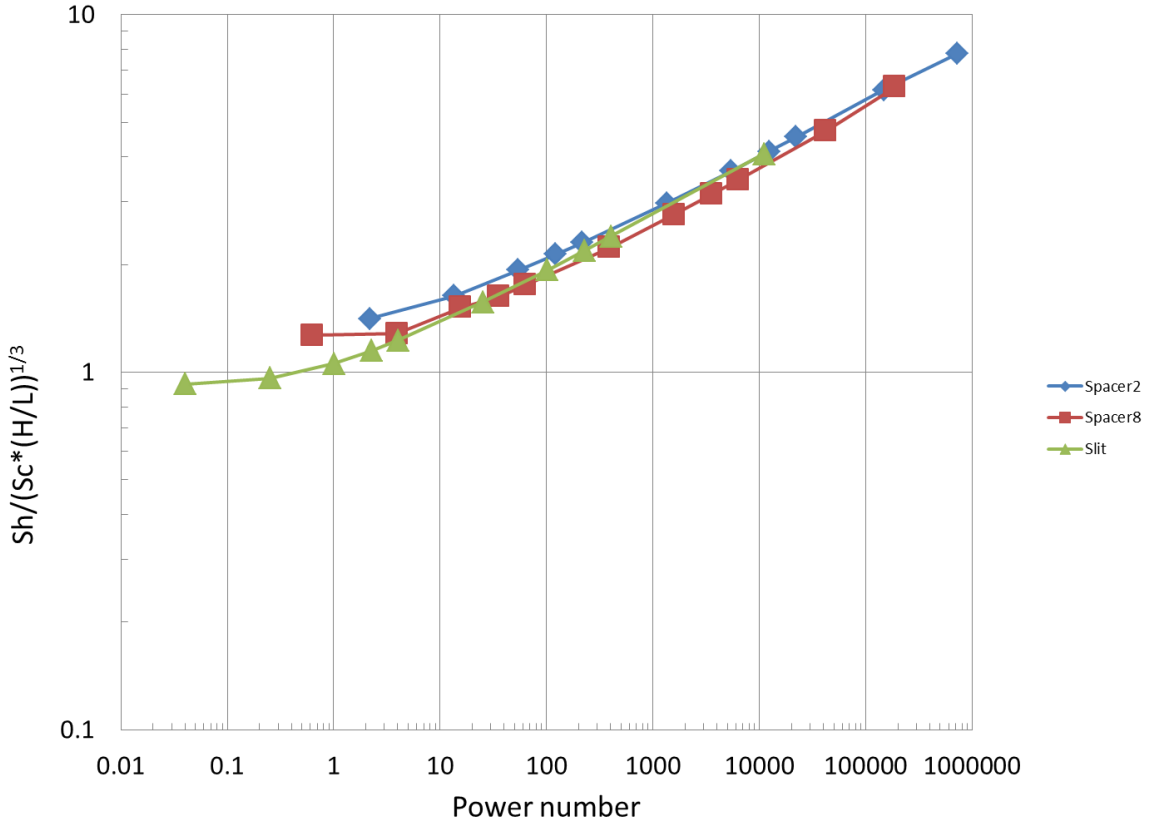

Figure 20. Sherwood number dependence on Power number for spacers 2 and 8 as well as an empty slit.

To observe mass transfer performance enhancement, flow channels that contain multiple spacer elements must be compared to empty channels of the same length. The distance between elements is an additional design parameter. To evaluate the effect of this parameter, simulations were performed for spacers 2 and 8 with a variable spacing between elements. Figure 21

illustrates the spacings considered for spacer 2; similar spacings were used for spacer 8.

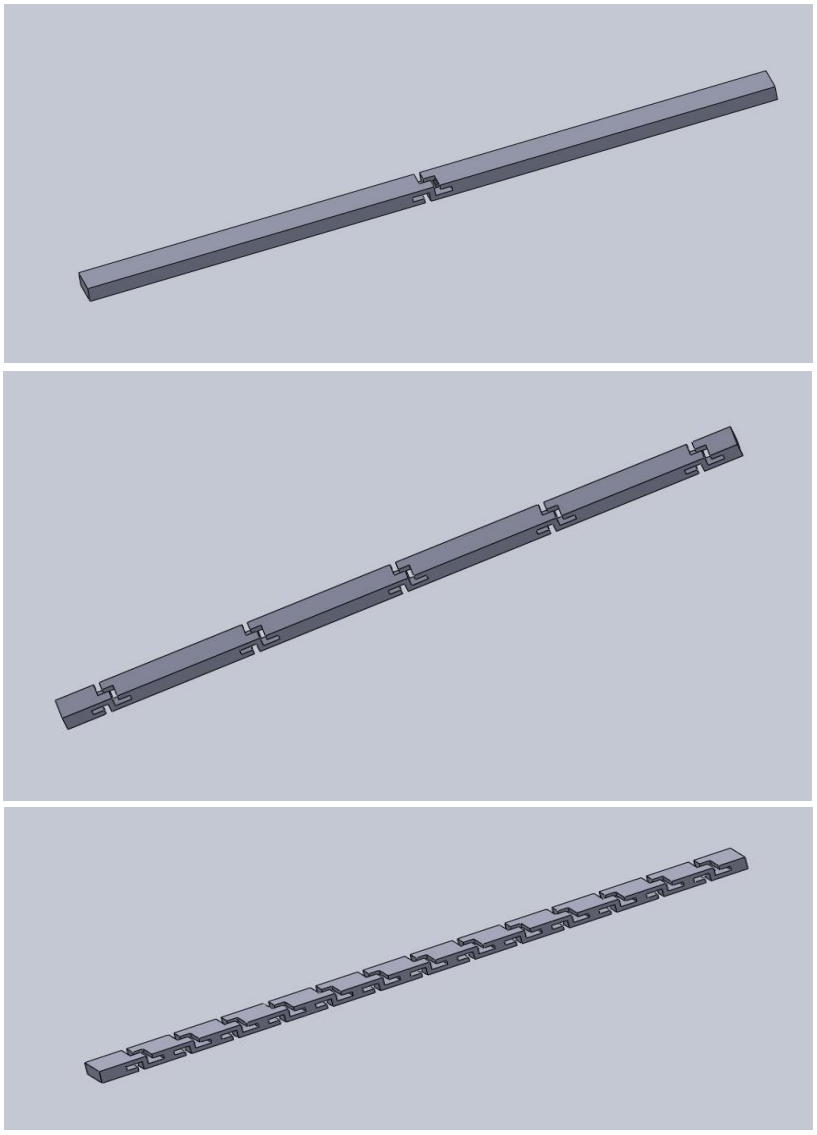

Figure 21.Spacer spacings simulated. The number of spacer elements considered were: (a) one, (b) five, and (c) thirteen.

The overall flow channel length is equal to the length of the experimental channel described in the experimental section and the spacer numbers correspond to spacings that could be realized experimentally.

Simulation results for spacer 2 are reported in Figure 22 as the dependence of Sherwood

number on Graetz number.

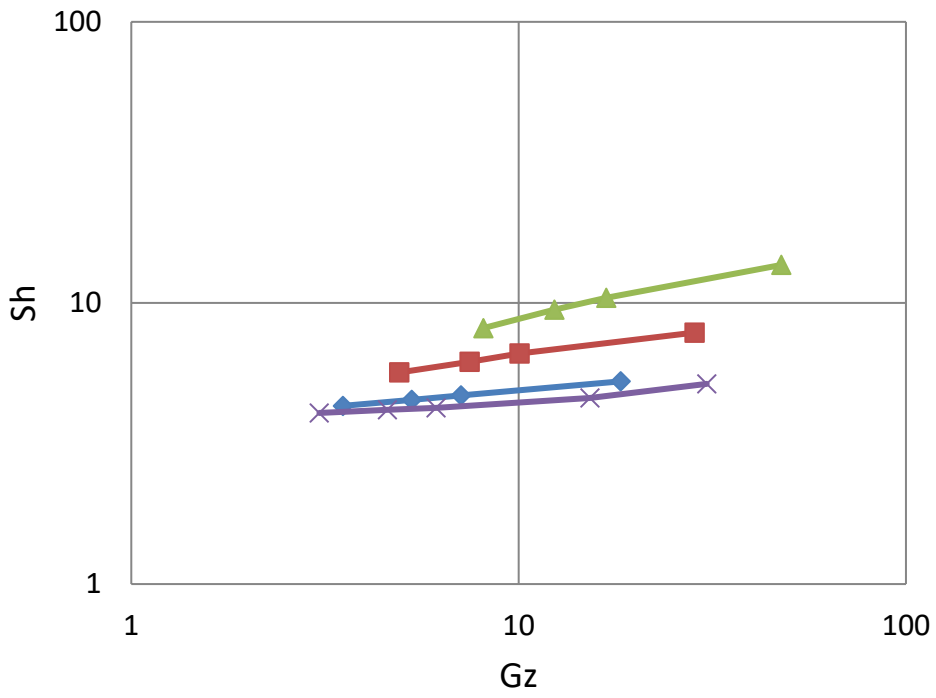

Figure 22. Dependence of Sherwood number on Graetz number for spacer 2. The lines correspond to: cross – slit; diamond – one spacer; square – five spacers; and triangle – thirteen spacers. The simulation domains are illustrated in Figure 21.

Figure 22 indicates that mass transfer for a single spacer is nearly identical to that for an empty channel as anticipated. Increasing the number of spacers increases the mass transfer coefficient since fluid mixing occurs more frequently. The mass transfer coefficient for thirteen spacers is nearly a factor of three larger than for a single spacer or empty channel. Similar results were obtained for spacer 8.

The increase in mass transfer coefficient comes at the expense of increased pressure drop. The dependence of friction factor on Reynolds number is illustrated in Figure 23. The pressure drop increases by nearly an order of magnitude for thirteen spacers relative to an empty channel.

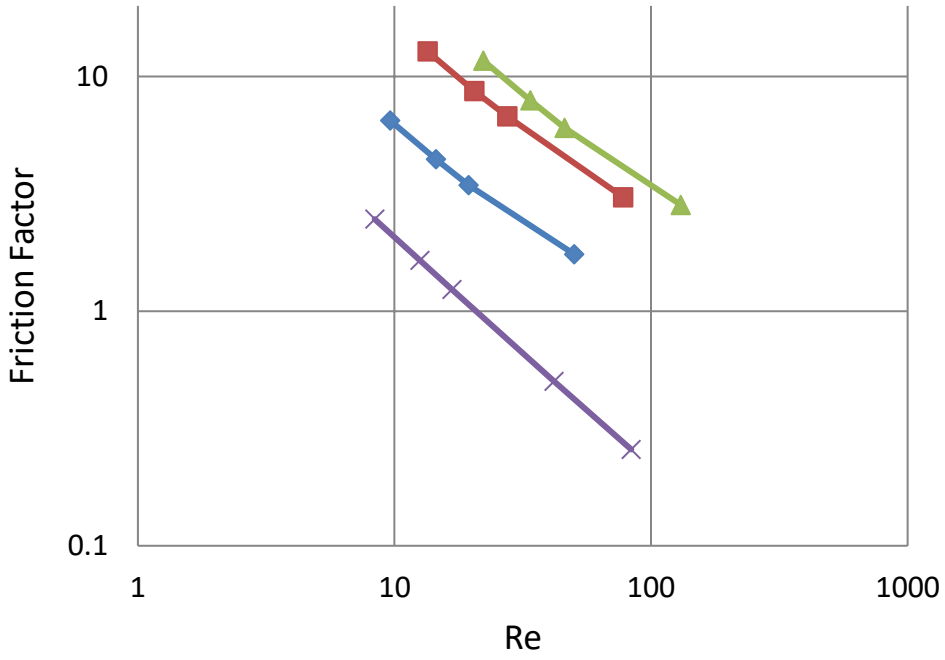

Figure 23. Dependence of friction factor on Reynolds number for spacer 2. The lines correspond to: cross – slit; diamond – one spacer; square – five spacers; and triangle – thirteen spacers. The simulation domains are illustrated in Figure 21.

Figure 24 illustrates the dependence of Sherwood number, scaled by the Schmidt number and channel height to length ratio raised to the one-third power, on the Power number. The scaled Sherwood number and Power number nominally are functions only of the Reynolds number. Therefore, Figure 24 provides a comparison of mass transfer performance (i.e., Sherwood number) for the various spacer filled channels at a fixed power input (i.e., Power number).

Figure 24 indicates that increasing the Reynolds number or Power number leads to an increase in Sherwood number and mass transfer performance. For a fixed power input, the addition of a single spacer element has no effect on mass transfer. However, performance improves as the number of spacer elements increases.

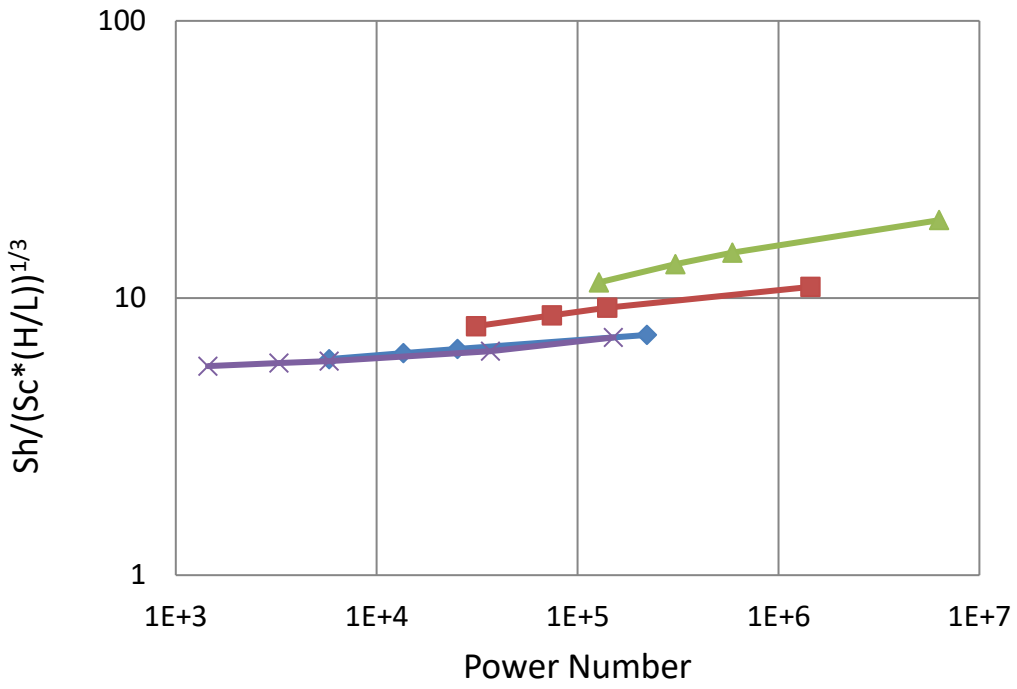

Figure 24. Dependence of scaled Sherwood number on Power number for spacer 2. The lines correspond to: cross – slit; diamond – one spacer; square – five spacers; and triangle – thirteen spacers. The simulation domains are illustrated in Figure 21.

Interestingly, the results for spacer 8 are nearly identical to spacer 2 indicating the trade-off between mass transfer and pressure drop for the two spacers does not affect performance at a fixed power input. This relative insensitivity to design parameters suggests extensive optimization of spacer design may not be necessary to optimize performance.

Figure 25 illustrates the effect of distance between spacer elements on the mixing cup average temperature within the flow channel for spacer 2. The equivalence of heat transfer to mass transfer for transport of a dilute solute was discussed previously. This equivalence is based on the substitution of temperature for concentration in the conservation equations. Thus, temperature variations and gradients are equivalent to concentration changes and gradients.

The effects of spacer elements on the mixing cup temperature gradient, and associated

heat transfer rate, are clearly evident. Relative to the results for an empty channel, the temperature profile for a single element follows the empty channel curve until reaching the spacer element at a length of ~0.07 m where a near step-change decrease occurs. Likewise, sudden temperature drops are identifiable for the results obtained with five and 13 spacer elements for each spacer element. The magnitude of the change is largest for the first element and decreases with subsequent elements.

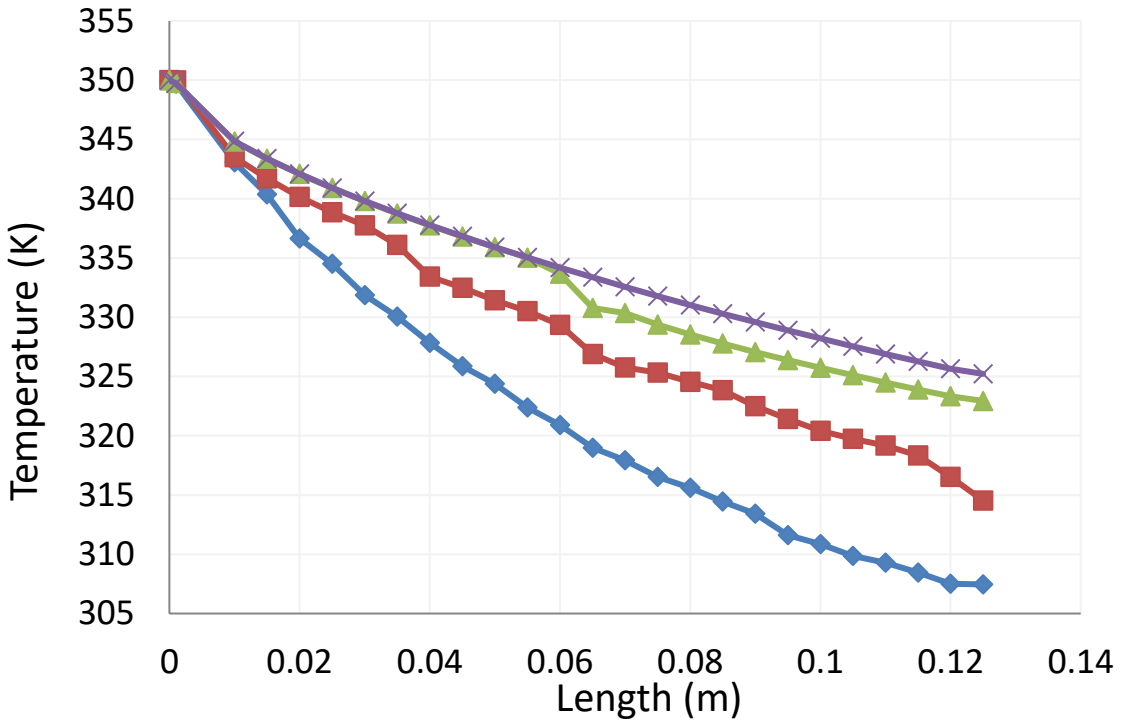

Figure 25. Effect of distance between spacer elements on temperature changes within the flow channel for spacer 2. The results correspond to: purple x – empty channel; green triangle – single spacer element; brown square – five equally spaced elements; and blue diamond – 13 equally spaced elements.

Figure 26 illustrates the temperature profile in two planes along the flow direction with a single spacer 2 element in the flow channel. The growth of the thermal boundary layer before the first spacer element is evident as well as the movement of the boundary layer to the middle of the

flow channel upon flowing through the spacer. The fluid adjacent to the membrane surface is replaced by fluid from the middle of the flow channel.

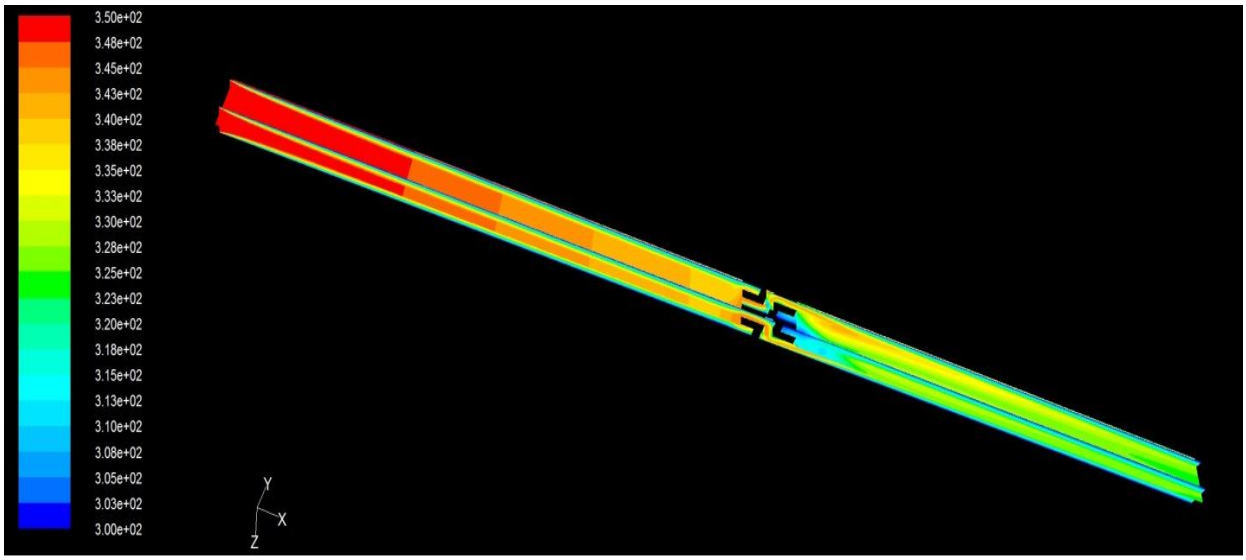

Figure 26. Temperature profile within two cross-sections along a flow channel containing a single spacer 2 element. Red indicates the highest temperatures and blue the lowest. Flow is from the upper left hand corner to the lower right hand corner.

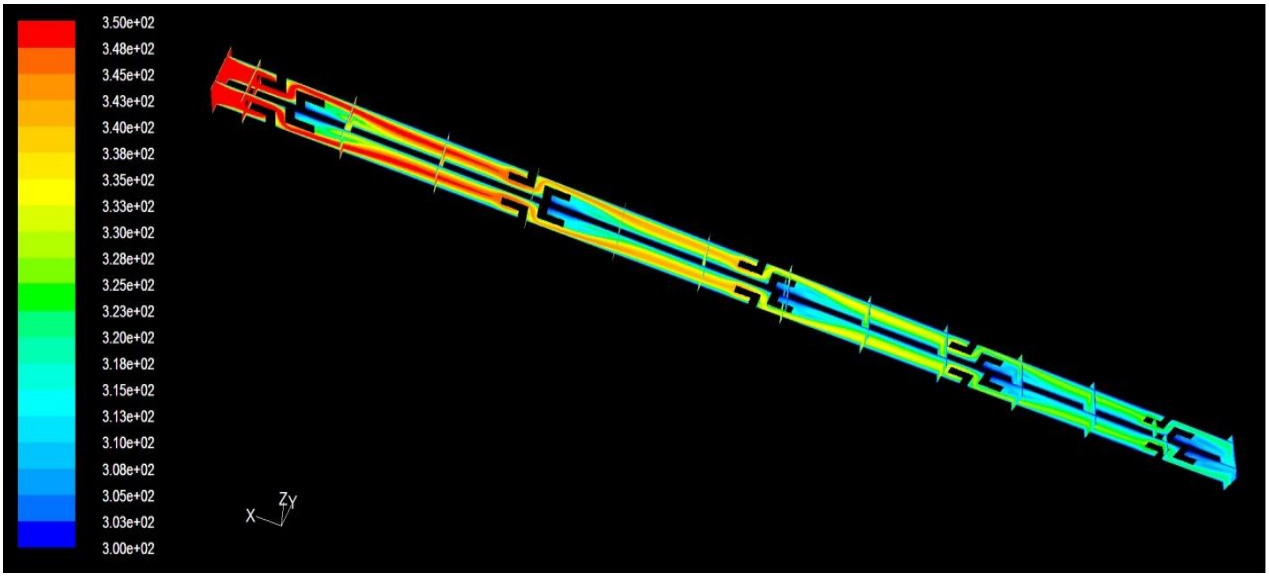

Figure 27. Temperature profile within two cross-sections along a flow channel containing five spacer 2 elements. Red indicates the highest temperatures and blue the lowest. Flow is from the upper left hand corner to the lower right hand corner.

Figure 27 illustrates the temperature profile in two planes for a channel containing five spacer 2 elements. The temperature boundary layer grows before each spacer element, is moved to the middle of the flow by the spacer element, and is replaced by fluid from the middle of the flow channel. This repeated mixing leads to the dramatic increases in heat transfer rates that are observed.

Figure 28 illustrates the temperature profiles for a channel containing 13 spacer 2 elements. As in Figures 26 and 27, each spacer element moves fluid from within the boundary layer to the middle of the flow channel and replaces it with fluid from the middle of the flow channel.

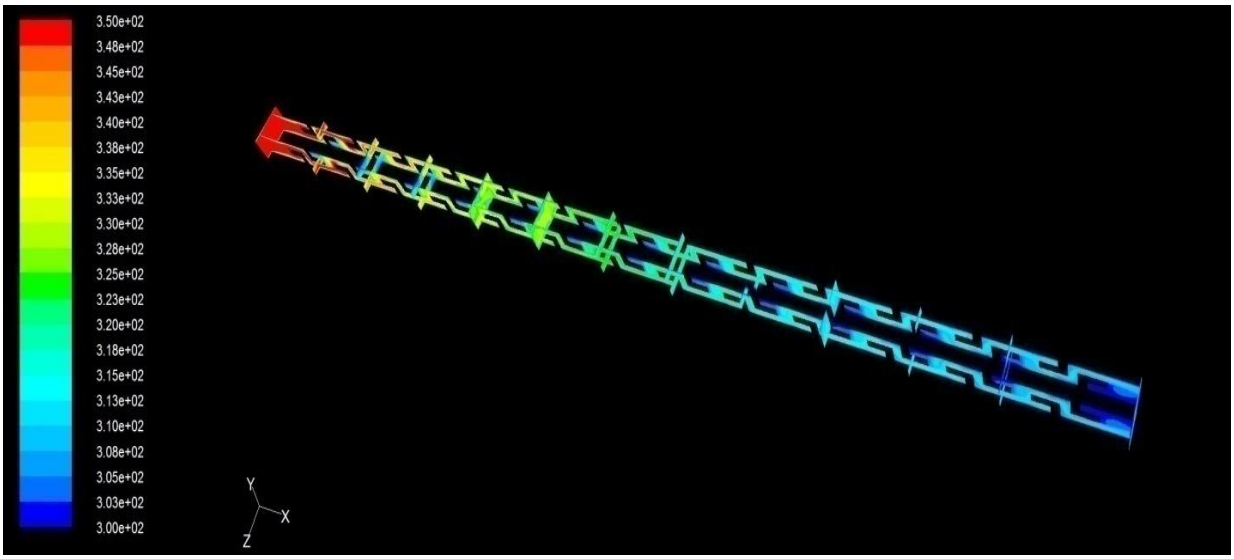

Figure 28. Temperature profile within two cross-sections along a flow channel containing 13 spacer 2 elements. Red indicates the highest temperatures and blue the lowest. Flow is from the upper left hand corner to the lower right hand corner.

The temperature profiles for a single spacer 8 element are illustrated in Figure 29. The temperature variations are qualitatively similar to those in Figure 26 for a single spacer 2

element. However, heat transfer coefficients are lower when space 8 is used.

Figure 30 illustrates the origin of this performance difference. To allow fluid flow from the upper part of the flow channel to the lower part, fluid is forced laterally, or in a cross-flow direction to the primary flow direction, and through an opening connecting the upper and lower parts of the flow channel. The length of this cross-flow region is longer for spacer 8 than for spacer 2.

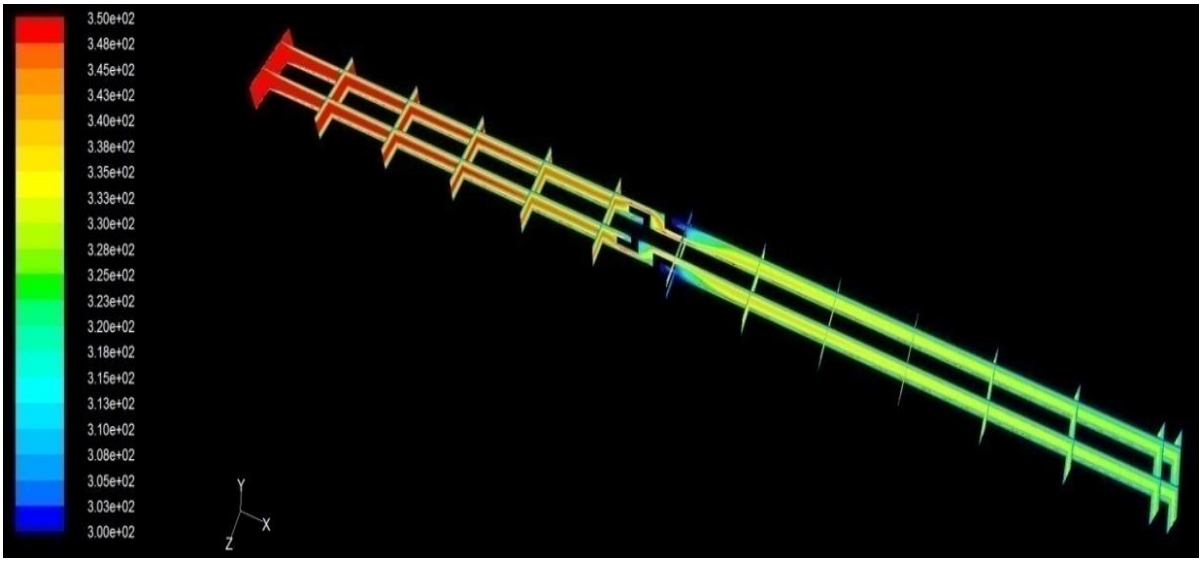

Figure 29. Temperature profile within two cross-sections along a flow channel containing one spacer 8 element. Red indicates the highest temperatures and blue the lowest. Flow is from the upper left hand corner to the lower right hand corner.

Cross-flow results in regions where velocities and velocity gradients are lower. In these regions heat transfer rates also are lower as the fluid contacts the membrane for a longer period of time and velocities approach zero at the middle of the cross-flow region. Consequently, the fluid temperature more closely approaches that of the boundary which reduces the driving force for heat transfer.

The effect of this on the temperature field is illustrated in Figure 31. In the down-stream

cross-flow region highlighted, the temperature is lower over a larger area (as indicated by a large dark blue region) for spacer 8 than for spacer 2. The lower temperature is due to the larger cross-flow region in spacer 8 which leads to longer residence times and allows the fluid temperature to approach more closely the temperature of the bounding membrane surface. While spacer 8 provides lower heat transfer coefficients, it also generates lower pressure drops. Pressure drops are lower as spacer 8 possesses more open area for flow through it.

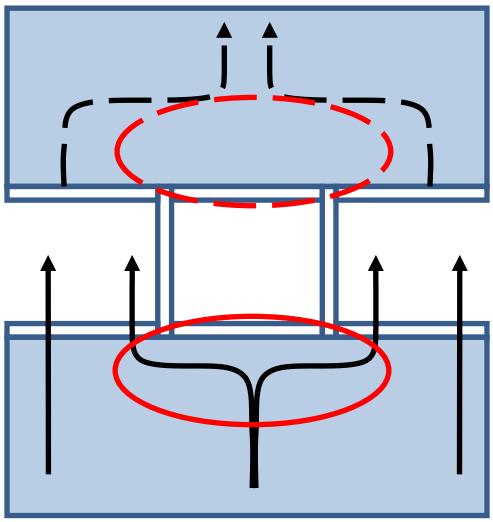

Figure 30. Top view of the fluid streamlines through a spacer element. Solid lines indicate streamlines are visible from the top and dashed lines indicate streamlines are not visible. The circled areas are the cross-flow regions: one in the upper part and one in the lower part of the flow channel. Similar regions are visible from the bottom.

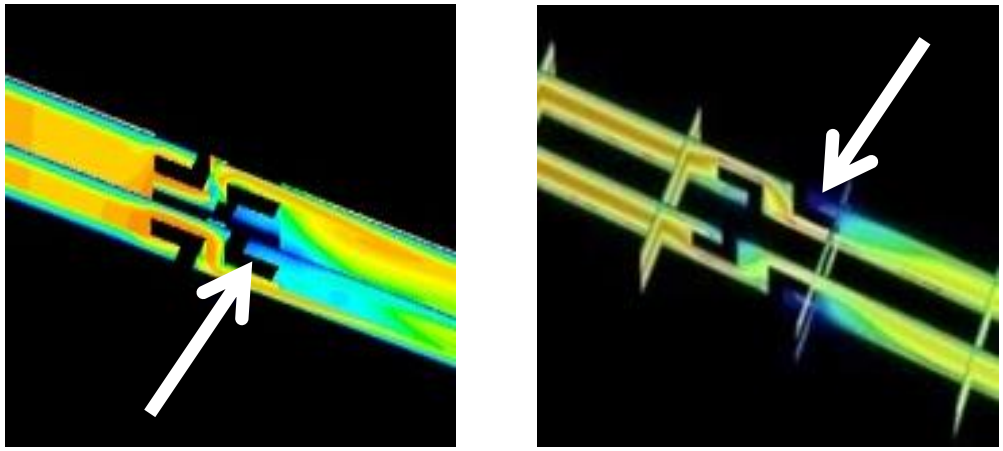

Figure 31. Temperature fields near the single spacer element: left – spacer2 and right – spacer 8. The arrows indicate regions behind a solid segment of the spacer where cross-flow normal to the primary flow direction occurs. The length of these cross-flow regions is greater for spacer 8 than for spacer 2.

Experimental Evaluation of Spacer Performance

Samples of spacers 2 and 8 with the dimensions indicated in Table 3 were fabricated for experimental evaluation. These spacers were selected because they provided the highest mass transfer coefficient (spacer 2) or lowest pressure drop (spacer 8) in the initial simulations of different designs. Experimental evaluation consisted of three components: 1) spacer manufacture, 2) mass transfer coefficient measurements, and 3) pressure drop measurements.

Spacer Manufacture

Quotes were requested from four stereolithography manufacturers: 1) Harvest Technologies, 2) Design Prototyping Technologies, 3) Metro Rapid Prototyping, and 4) Protocad. Harvest Technologies was selected because the purchase price was lowest and if quality was poor another manufacturer could have been used. The manufacturer was provided with a CAD drawing of a spacer strip designed to fill the width of an Osmonics SepaCF membrane cell. An example is

provided in Figure 32. The strip consists of the section illustrated in Figure 10 repeated 12 times.

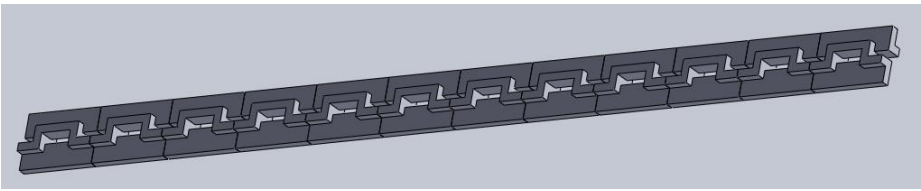

Figure 32. CAD drawing of spacer element.

To align and hold the spacer strips a fixed distance apart, the frame illustrated in Figure 33 was designed. The frame possesses a series of opposing notches that can accommodate the ends of the strips in Figure 32. The number of strips inserted into the frame determines the distance between spacer elements: filling every pair of opposing notches gives the minimum spacing while filling only the center pair gives the maximum spacing.

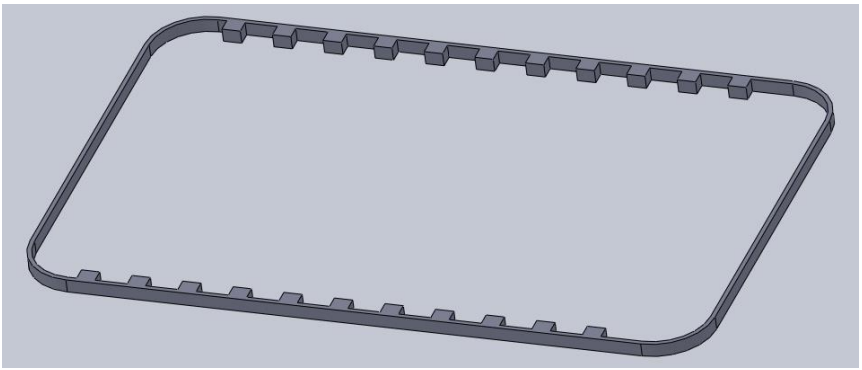

Figure 33. Frame to hold spacer elements.

Figure 34 illustrates the Osmonics Sepa CF cell with the spacer filled frame to be used in the experiments.

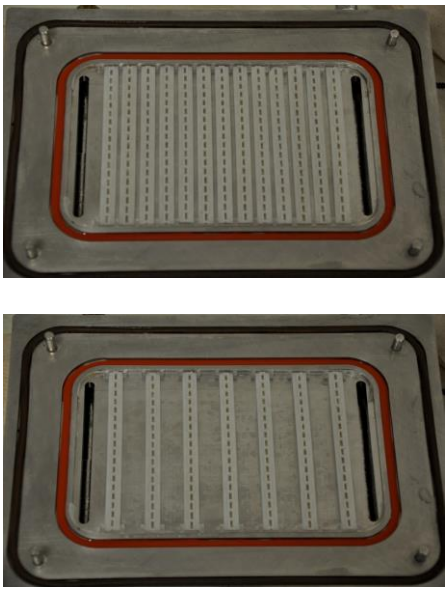

Figure 34. Osmonic Sepa CF feed channel filled with the static mixing spacer and frame illustrated in Figures 32 and 33. The top image is for the minimum inter-spacer spacing and the bottom for twice the minimum spacing.

Mass Transfer Coefficient Measurements

Experimental measurements of mass transfer coefficients were conducted for ultrafiltration of aqueous dextran solutions. The experimental system is similar to that used by previous researchers [Da Costa et al., 1991].

The experimental apparatus used to evaluate mass transfer performance is illustrated in Figure 35. The filtration cell is an Osmonics Sepa CF II cell. The cell consists of two 316 stainless steel blocks machined to create flow channels and fluid entry and exit ports. The two halves are held together in operation by an anodized aluminum cell holder that is pressurized using an external hydraulic hand pump.

The retentate and permeate flow channels are 165 mm wide and 213 mm long. The cell requires membranes 190 mm by 140 mm for sealing with Viton o-rings between the two flow channels. The cell is assembled by placing a feed spacer in the lower, feed flow channel; a

membrane on the feed spacer; a permeate spacer on the membrane; and the upper, permeate flow channel on the permeate spacer to complete the assembly. The assembled cell is slid into the cell holder and the holder pressurized before conducting experiments.

The feed solution is circulated through the feed channel using an ISMATEC MV gear pump. The feed inlet and outlet pressures are monitored by pressure gauges to determine the average retentate pressure and retentate channel pressure drop. The average retentate pressure is regulated using valve V-1. Valve V-2 is used to direct the permeate either to the feed tank to create a closed recirculating system or to a sample collector to determine flow rate by timed collection. Collected samples are returned to the feed tank to maintain a constant volume.

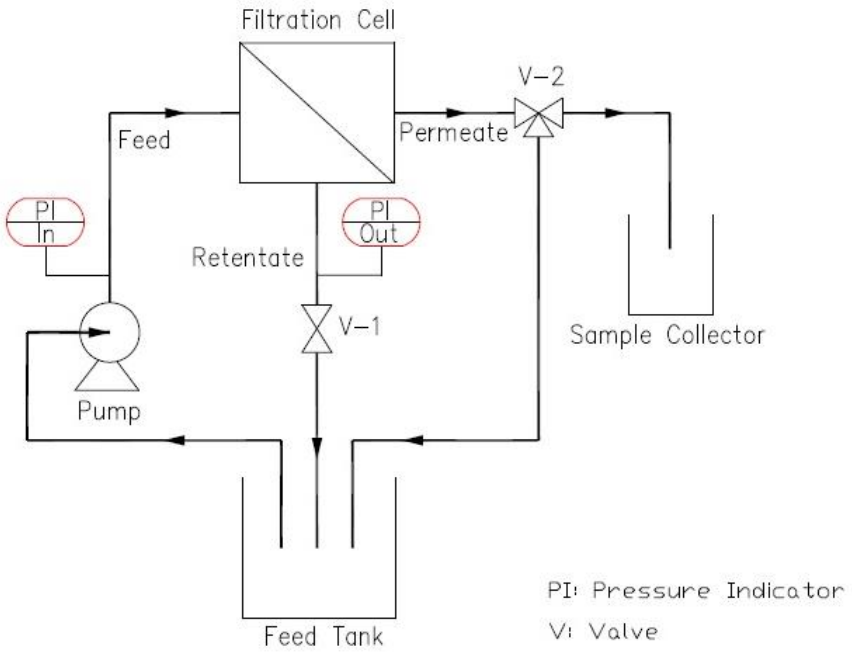

Figure 35. Experimental set-up used to evaluate mass transfer performance.

Experiments were conducted using an ultrafiltration membrane to concentrate aqueous solutions of dextran [Da Costa, et al., 1991]. Dextran with a molecular weight of 500,000 was

used to prepare solutions with a concentration of 5 kg/m^3 using deionized water. A polyethersulfone membrane with nominal molecular weight cutoff of 5000 Da (GE Infrastructure Water and Process Technologies) was used in the experiments.

The experimental protocol consists of the following steps:

1. determine the membrane pure water hydraulic permeability
2. determine water flux for a range of feed flow rates for the dextran solution
3. calculate effective mass transfer coefficient from water flux

The pure water measurement is used to determine the membrane hydraulic permeability from Equation (14):

$$J = L_p(\Delta P_{TM} - \Delta\pi_W) \tag{14}$$

where J is the measured flux, L_p the hydraulic permeability, ΔP_{TM} the average trans-membrane pressure difference, and $\Delta\pi_w$ is the osmotic pressure difference. The average trans-membrane pressure difference is given by Equation (15):

$$\Delta P_{TM} = \left(\frac{P_{Feed} + P_{Retentate}}{2}\right) - P_{atm} \tag{15}$$

where P_{Feed} is the feed pressure, $P_{Retentate}$ the exit retentate pressure, and the permeate channel is assumed open to the atmosphere with negligible pressure drop. For the pure water measurement the osmotic pressure difference is zero.

The hydraulic permeability calculated from the pure water flux measurement is used to calculate the osmotic pressure difference across the membrane from water flux measurements for the dextran solution using Equation (14). The concentration of dextran in the liquid adjacent to the membrane surface, C_W, is calculated from the known relationship between concentration and

osmotic pressure given by Equation (16):

$$\Delta\pi_W = 37.5C_W + 0.75C_w^2 + 0.00764C_W^3 \tag{16}$$

The wall concentration is used to calculate the average mass transfer coefficient from film theory using Equation (17):

$$J = hln(C_w/C_b) \tag{17}$$

where C_b is the bulk fluid dextran concentration.

Experimental mass transfer coefficients are reported in Figure 36 along with theoretical predictions for the static mixing spacer, an empty feed channel, and for the commercial spacer supplied by Osmonics. Mass transfer coefficients are reported non-dimensionally as Sherwood number scaled by the product of the Schmidt number and the channel height-to-length ratio raised to the one-third power to yield values expected to be a function of Reynolds number only.

Note that in the experiments only one side of the spacer is bounded by a membrane – the other side is bounded by an impermeable wall. The theoretical results in Figure 36 were obtained with this boundary condition in contrast to the results reported previously for a spacer bounded by two permeable membranes.

Although the experimental and theoretical results for the empty channel span different ranges of Reynolds number the results appear to lie along a common line and indicate good agreement. The experimental results obtained with the spacer supplied with the Sepa CF cell show a modest increase in mass transfer coefficient relative to an empty channel.

The experimental mass transfer coefficients for the static mixing spacer are approximately four times larger than for an empty channel and are significantly higher than the theoretical predictions. The difference between theory and experiment is attributed to the strong

dependence of fluid properties, in particular viscosity and diffusivity, on dextran concentration. The theoretical calculations assume all material properties are constant. Simulations can be performed for variable material properties but the results are difficult to generalize. Consequently, the literature commonly assumes theoretical results obtained in the absence of physical property variations can be used if the properties of the fluid adjacent to the membrane are used. Experimental results are non-dimensionalized and reported in Figure 38 based on this assumption.

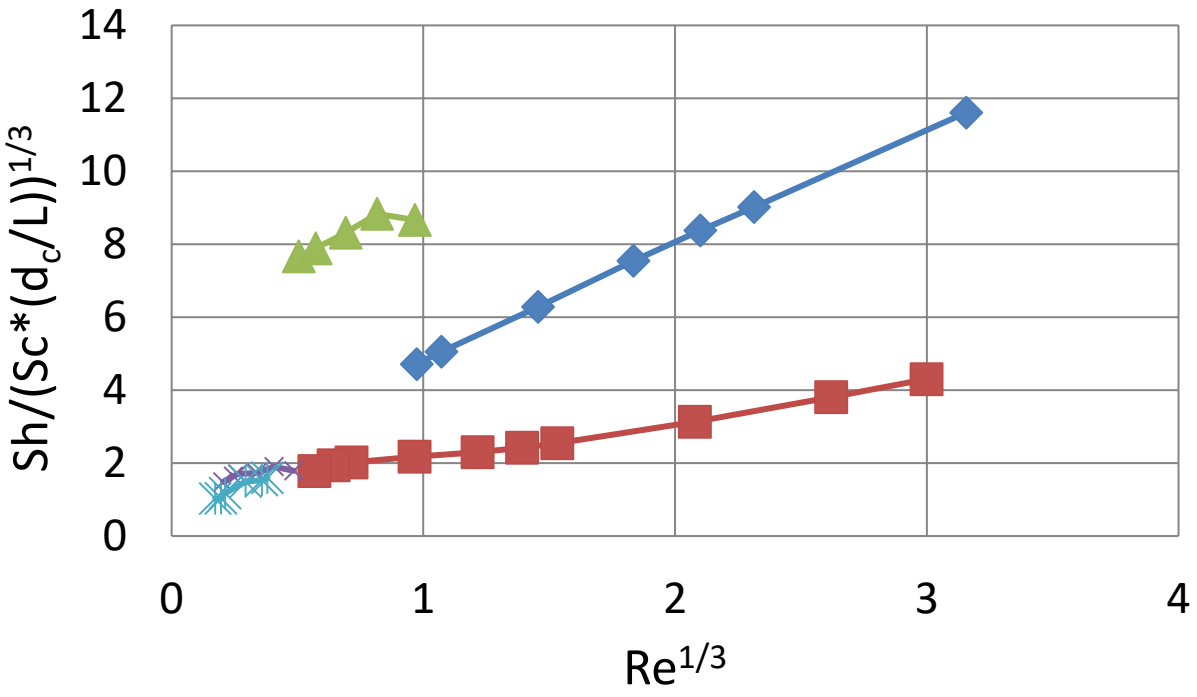

Figure 36. Dimensionless mass transfer coefficients as a function of Reynolds number. The symbols represent: theoretical (red square) and experimental (blue star) results for an empty channel, theoretical (blue diamond) and experimental (green triangle) results for 13 spacer 2 elements, and experimental (purple x) results for the spacer supplied with the cell.

The calculated values of the dextran wall concentration are provided in Figure 37. Use of

the static mixing spacer led to the lowest values of wall concentration which reflects the superior mixing it provides relative to an empty channel or the commercial spacer provided with the Osmonics test cell.

The values of wall concentration for all three spacers appear to fall on a common curve. This suggests the mixing that occurs in all three cases possesses some common characteristic that is captured by the Reynolds number. This may reflect the effective frequency with which growth of the concentration boundary layer is disrupted. The frequency increases with use of the commercial spacer and is highest with the static mixing spacer relative to an empty channel.

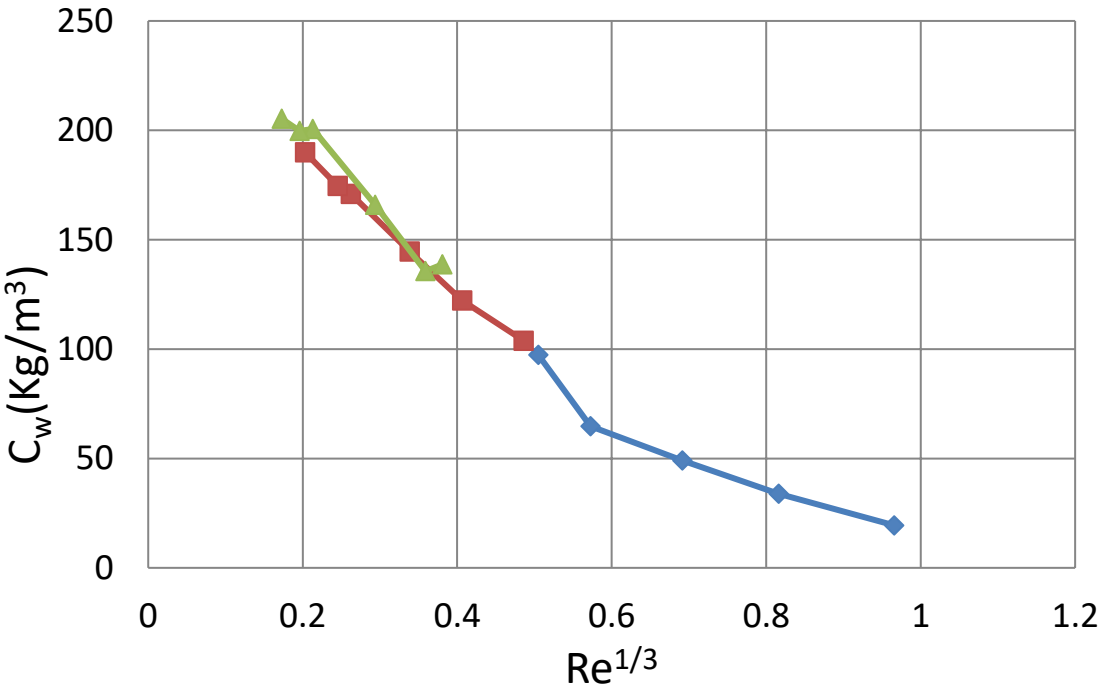

Figure 37. Calculated values of the dextran wall concentration as a function of the Reynolds number. The symbols represent: green triangle – empty channel, brown square – spacer supplied with Osmonics cell, and blue triangle – 13 spacer 2 elements.

Figure 38 compares experimental and theoretical values for pressure drop for an empty

channel, the supplied spacer, and the static mixing spacer observed during the dextran filtration experiments. The agreement between theory and experiment for the empty channel is much poorer for pressure drop than for mass transfer coefficient. The agreement for the static mixing spacer also is poor. As anticipated, the experimental pressure drops for both spacers were higher than for the empty channel and the static mixing spacer gave the largest values.

The differences between theory and experiment are attributed primarily to the large variation in dextran concentration within the flow channel. Figure 37 indicates the dextran concentration can vary by a factor of 40 (from 5 to 200 kg/m^3) which leads to a large viscosity variation that the simulations do not include.

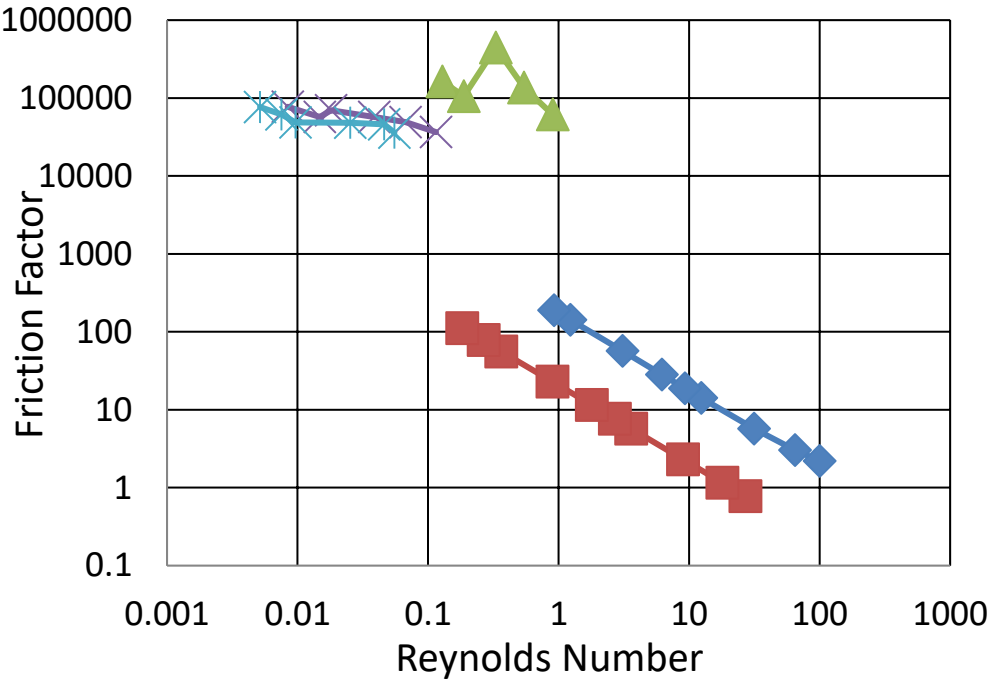

Figure 38. Dimensionless pressure drop as a function of Reynolds number: theoretical (red square) and experimental (blue star) results for an empty channel, theoretical (blue diamond) and experimental (green triangle) results for the static mixing spacer, and experimental (purple x) results for the supplied spacer.

Figure 39 illustrates the dependence of the scaled Sherwood number on the Power

number and allows comparison of mass transfer performance at a fixed power input. The experimental curves indicate that mass transfer coefficients increase with the addition of a spacer. The static mixing spacer gives the largest increase at a given Power number or energy input – the mass transfer coefficient is approximately four times greater than an empty channel over the range of Power numbers shown. This result suggests that the static mixing spacer has significant potential to improve mass transfer performance economically.

For both the empty channel and static mixing spacer, the agreement between theory and experiment is fair despite the poor agreement for pressure drop observed in Figure 38. The differences in the predictions for mass transfer coefficient and pressure drop appear to compensate for each other.

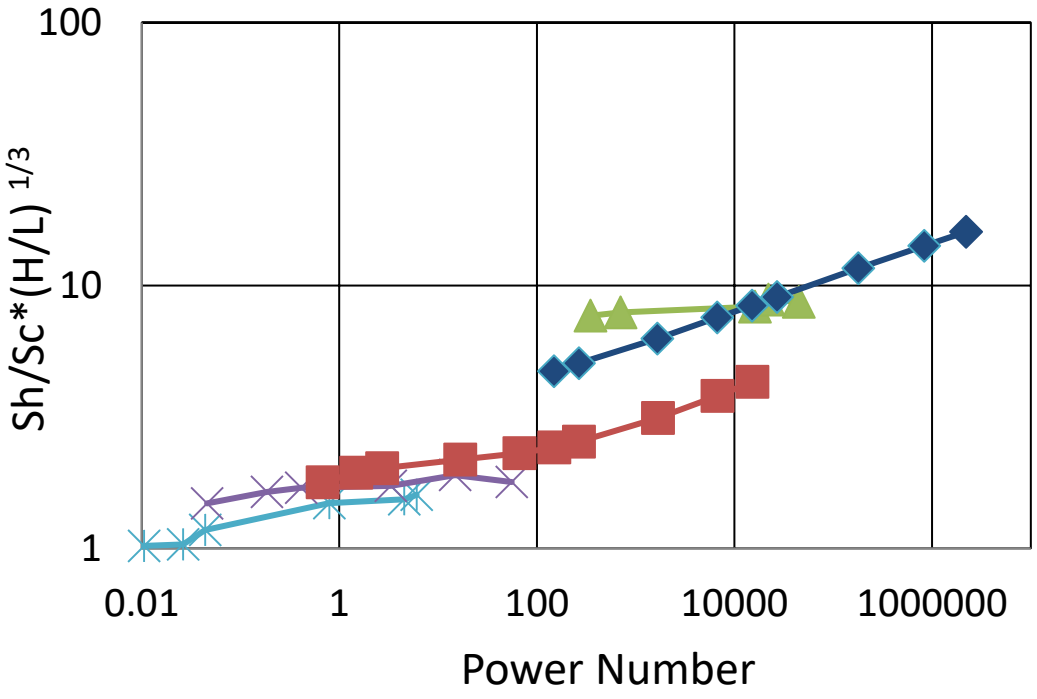

Figure 39. Dimensionless mass transfer coefficient as a function of Power number: theoretical (red square) and experimental (blue star) results for an empty channel, theoretical (blue diamond) and experimental (green triangle) results for the static mixing spacer, and experimental (purple x) results for the supplied spacer.

The data analysis required to compute mass transfer coefficients assumes 100% dextran rejection. To confirm this, proton nuclear magnetic spectroscopy was used to check for the presence of dextran in the feed and permeate.

Figure 40 illustrates the spectrum obtained for the feed and Figure 41 the spectrum for the permeate. Peaks characteristic of dextran protons are found in the 3.20- 3.80 ppm range for the feed but no peaks are present in the permeate spectrum. Therefore, dextran transport is not detectable.

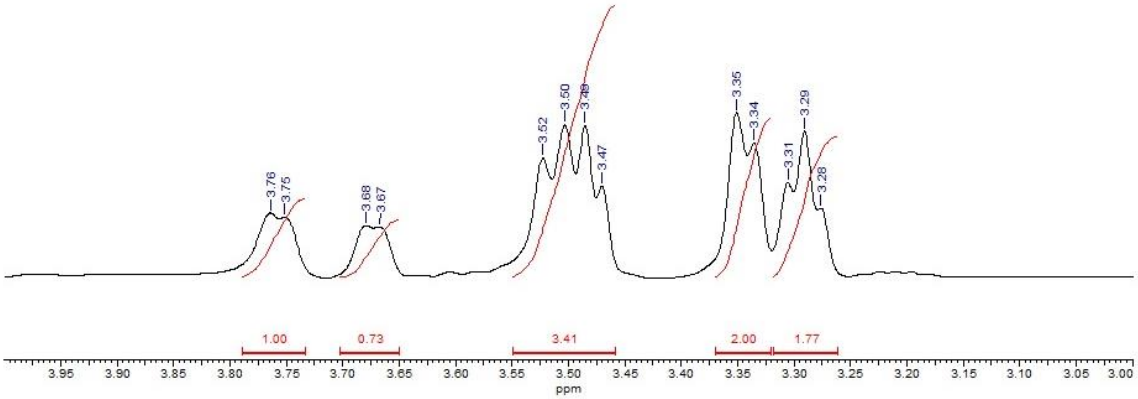

Figure 40. NMR spectrum of dextran feed solution.

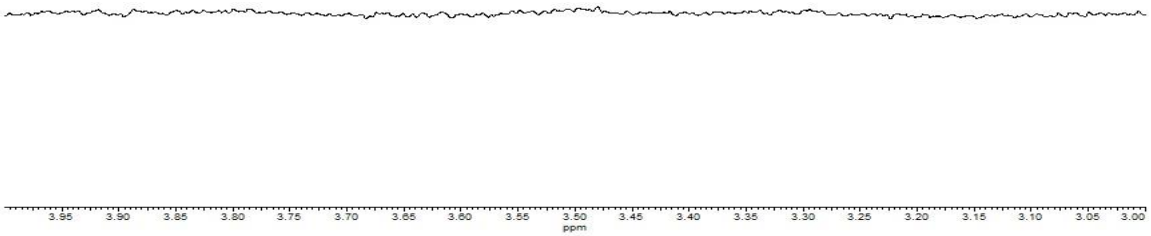

Figure 41. NMR spectrum of permeate.

Pressure Drop Measurements

Pressure drops measured during the ultrafiltration experiments reflect the variation in viscosity that occurs due to the concentration gradients in the flow channel as well as the change in flow rate that occurs due to permeation. To eliminate these confounding effects, experimental measurements of pressure drops for pure water in the absence of permeation were performed.

The experimental apparatus illustrated in Figure 42 was developed to perform the pressure drop measurements. The Osmonics Sepa CF II test cell is assembled as described previously. The assembled cell is slid into the cell holder and the holder pressurized before conducting experiments. The permeate channel was filled with water prior to the experiments and the outlet port closed during the experiments to prevent permeation across the membrane.

To measure pressure drops, vertical water filled tubes were attached to the flow channel inlet and outlet. The height of the liquid in each tube provides a direct measure of the hydrostatic pressure at the bottom of the tube. The difference in height between the two tubes can be used to calculate the pressure drop between the inlet and outlet.

Experimental measurements of pressure drop are reported as dimensionless values of friction factor as a function of Reynolds number in Figure 43 for an empty channel, spacer 2, and spacer 8. Figure 43 indicates that in all cases the experimental pressure drops are significantly higher than theoretical predictions. However, the theoretical and experimental values appear to approach each other as the Reynolds number decreases. The slopes of the experimental curves change from a value of nearly zero at high Reynolds number to a value of approximately one at low Reynolds numbers which is expected for laminar flow through closed ducts and consistent with theoretical predictions.

We hypothesize the change in slope at higher Reynolds numbers is due to inertial effects

associated with fluid entry and exit from the flow channel. The pump is connected to the cell by cylindrical tubing. The fluid enters the flow channel by flowing from the tubing into a cylindrical distribution channel within the cell and then through a distribution slit. The fluid must change flow direction twice before it enters the spacer filled flow channel: 1) to enter the distribution slit from the distribution channel the fluid must change flow direction by 90 degrees and 2) to enter the spacer filled flow channel from the distribution slit the fluid must change flow direction by 90 degrees again. These changes are accompanied by inertial pressure drops (form drag) which are proportional to velocity squared and therefore would give a constant value for the friction factor in the absence of viscous drag.

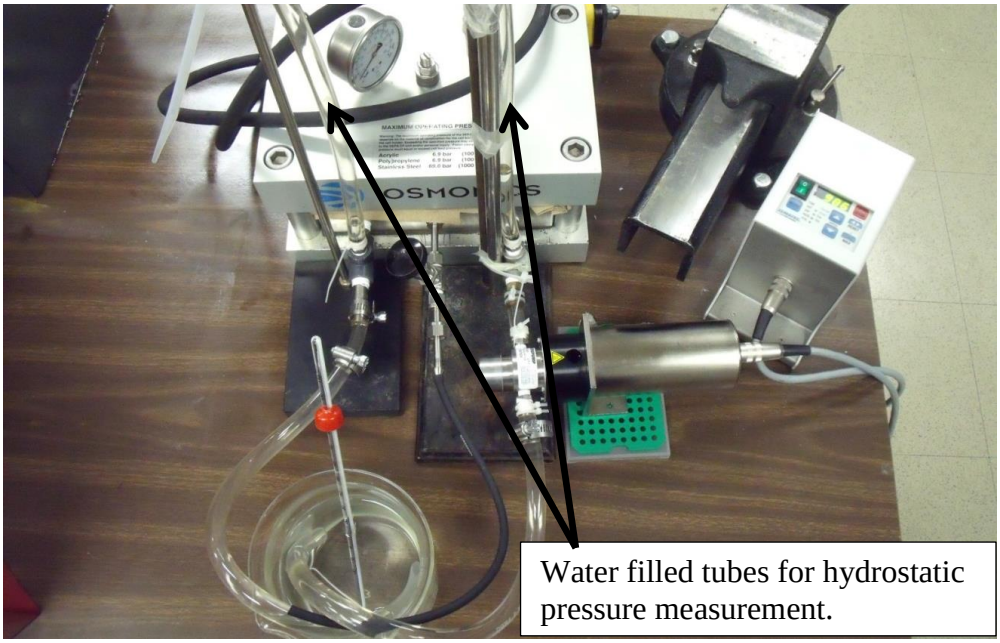

Figure 42. Experimental apparatus used to measure pressure drops for water flow through the spacer filled channel. Vertical, water filled tubes are used to measure the pressure at the inlet and outlet to the flow channel.

The inertial (entry and exit) contribution to the pressure drop increases as velocity increases because of its dependence on the velocity squared. Therefore, one would expect

experimental measurements of the overall pressure drop to approach theoretical predictions of the viscous pressure in the flow channel at sufficiently low Reynolds numbers as observed in Figure 43.

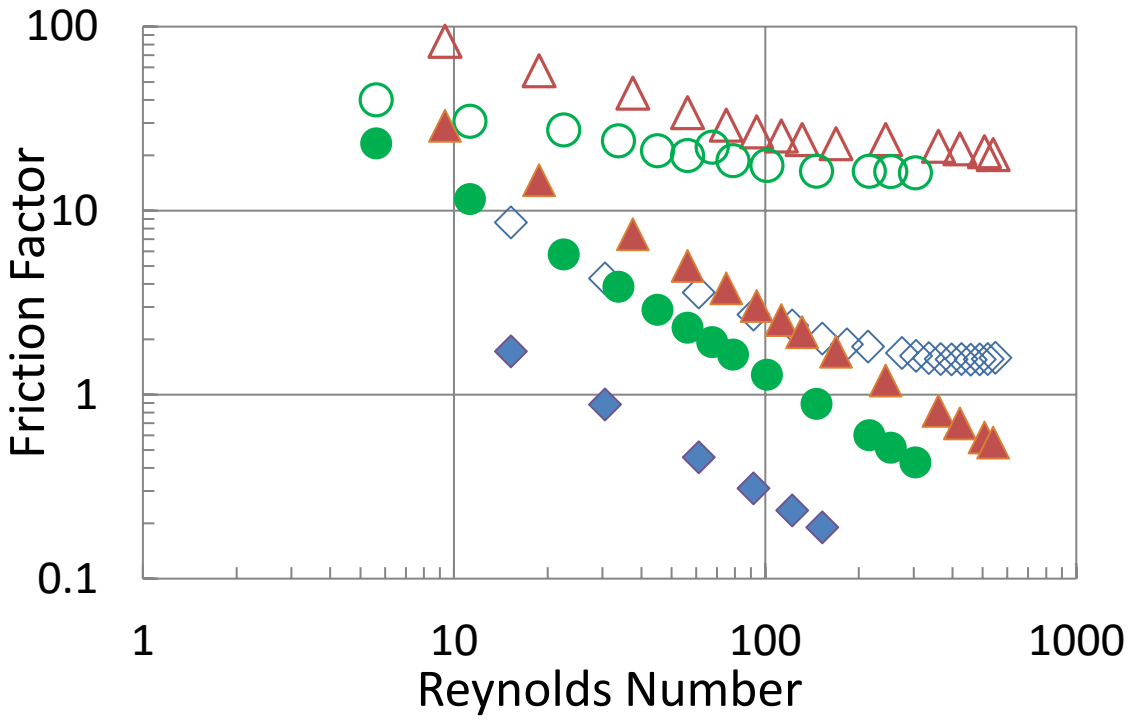

Figure 43. Friction factor as a function of Reynolds number. The symbols indicate values for: diamond – empty channel; circle – spacer 2; and triangle – spacer 8. Filled symbols represent theoretical predictions and empty symbols experimental measurements.

Flow Visualization

To visualize flow through the spacer, an experimental procedure to image fluid displacement was developed using Computed Tomography (CT). A Toshiba Aquilion 16 CT scanner located on the Health Science Campus of the University of Toledo was used in the experiments. This third generation multi-slice helical scanner is capable of acquiring 16 parallel rows of data per rotation

in helical mode. The instrument was used in a dynamic continuous scan mode in which four slices were imaged every second for a prescribed period of time.

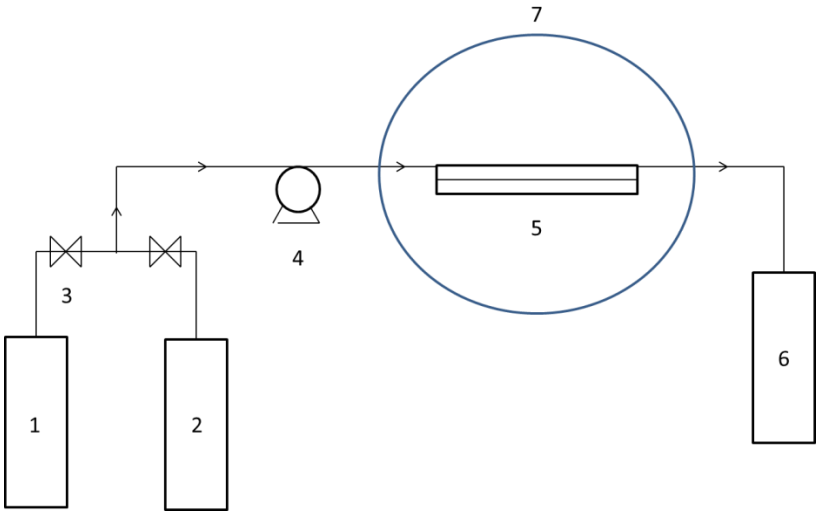

Figure 44. Experimental set-up for flow imagining using CT. The numbers correspond to: 1) pure water reservoir, 2) 0.1 M potassium iodide (KI) solution reservoir, 3) control valves, 4) peristaltic pump, 5) spacer test cell, 6) waste reservoir, and 7) rotating x-ray source and detector ring of CT scanner.

The experimental apparatus is illustrated in Figure 44. A custom membrane test cell constructed from polyethylene blocks was used in the experiments since metallic materials of construction cannot be present along the x-ray path; metallic objects introduce scattering that precludes accurate imaging. The cell possesses dimensions identical to that of the Osmonics Sepa CF test cell but also allows the introduction of a permeate sweep at one end of the permeate flow channel and withdrawal of the permeate product from the opposite end. For the experiments reported here, the permeate channel was filled with water initially and the inlet and outlet ports closed to prevent permeation.

CT imaging relies on measuring x-ray transmission through the interrogation volume for a large number of incident beam angles. The x-ray source and opposing linear detection array are located on a ring that rotates at high velocity around the object to allow rapid data acquisition. In dynamic mode, images can be obtained approximately once per second. The rate of image acquisition and total number of images is limited primarily by cooling of the x-ray source.

The raw transmission values are converted to absorbance values within a set of volume elements that fill the interrogated volume using reconstruction algorithms provided by the manufacturer. Absorbance values are reported as CT numbers which can be visualized by assigning a color or gray level to different value ranges and generating an image from the assigned colors.

The experimental procedure consists of:

1. filling the feed channel with water and displacing the initially entrapped air
2. pumping water at a prescribed rate through the feed channel; a flow rate of ~400 ml/min was used
3. manually switching the feed reservoir from water to a 0.1 M KI solution
4. obtaining a set of dynamic images for a period of time that allows the KI solution to displace the water from the feed channel
5. manually switching the feed reservoir from the 0.1 M KI solution back to water
6. obtaining a set of dynamic images for a period of time that allows the water to displace the KI solution from the feed channel

The sequence of images obtained upon displacing water with 0.1 M KI is illustrated in Figure 45. The white regions in the 0 s image correspond to the plastic elements of the static mixing spacer 8. The leading and trailing edges are clearly visible in the first and last element while the cross-

section of the middle element appears to lie within one wall of the chimneys through which fluid flows from the top of the flow channel to the bottom or vice versa.

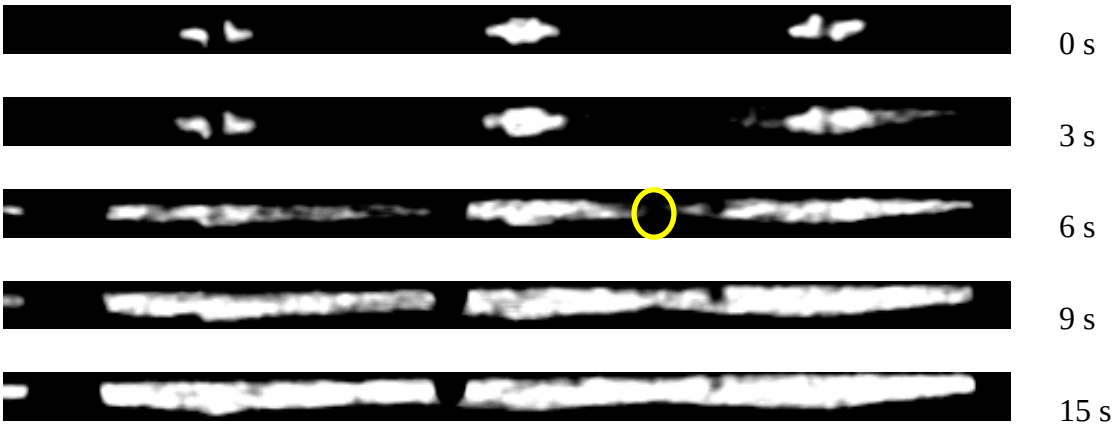

Figure 45. Displacement of water by KI in a static mixing spacer filled channel. Flow is from right to left. KI concentration decreases as the color changes from white to black. The numbers indicate relative time in seconds. The white regions in the 0 s image correspond to the plastic elements of the spacer. The yellow circle indicates a salt free region between the far right and middle spacer elements.

Figure 45 clearly illustrates fluid passage through the flow channel as the color changes from black to white. Movement of the displacement front indicates relative velocity through the channel. The 3 s image suggests fluid enters along the top part of the channel (a whiter region exists near the upper surface) but is moved to the center of the flow channel after passing the first spacer element as expected from the static mixing spacer design. The images at later times indicate an air bubble or pocket is trapped behind the second spacer element and does not move during the experiment.

The sequence of images obtained upon displacing 0.1 M KI with water is illustrated in Figure 46. The white regions in the 6 s image correspond to the same plastic elements of the spacer as in the 0 s image of Figure 45.

The air pocket present in Figure 45 remains unchanged in Figure 46 during the second displacement experiment. Figure 46 suggests fluid along the top and bottom boundaries is displaced faster than in the middle of the flow channel as expected for the static mixing spacer design.

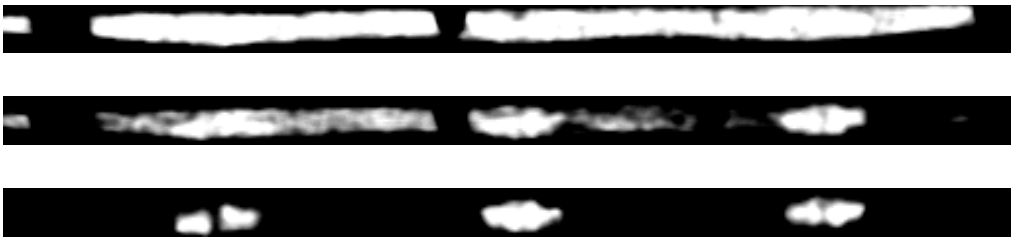

Figure 46. Displacement of KI by water in a spacer filled channel. Flow is from right to left. KI concentration decreases as the color changes from white to black. The numbers indicate relative time in seconds. The white regions in the 6 s image correspond to the plastic elements of the spacer.

Figures 45 and 46 both suggest that fluid displacement is not uniform along the width of the flow channel (i.e., in the direction normal to the principal flow direction) as one would expect from the cross-flow required to move fluid into the chimneys of the spacer illustrated in Figure 30. This is especially evident in the salt free region that exists between the far right spacer element and the middle element of the 6s image in Figure 45. This salt free region lies between regions of high salt concentration indicating the flow does not occur solely from right to left within the cross-section.

Conclusions

A novel static mixing spacer for planar flow channels has been evaluated experimentally and theoretically. The spacer moves fluid adjacent to the surfaces of the flow channel to the middle of the channel and fluid from the middle to the surface. Such mixing should help reduce

concentration polarization. Additionally, this mixing will reduce the concentration of rejected species adjacent to the membrane surface which should help mitigate fouling due to precipitation or gelation. The mixing is fundamentally different from that produced by conventional spacers that rely upon fluid vorticity or turbulence for mixing.

Theoretical simulations of the spacer indicate significant enhancement in mass transfer coefficients is possible relative to an empty channel. The enhancement comes at the cost of increased pressure drop. However, for a given power input, the static mixing spacer can enhance mass transfer coefficients by a factor of three or more relative to an empty channel.

Samples of the spacer were fabricated using stereolithography. The spacer was assembled from strips of the mixing elements placed in a support frame. Spacer performance in terms of pressure drop and effective mass transfer coefficient was evaluated for the ultrafiltration of aqueous dextran solutions. The experimental results confirm the theoretical predictions: mass transfer coefficients were a factor of four higher for a given power input relative to an empty channel and more than a factor of two higher relative to a commercial spacer.

Additional measurements of pressure drop suggest flow through the test cell possesses an inertial component from fluid entry and exit into the cell that can be significantly larger than the viscous pressure drop through the spacer filled channel. A test cell would have to be constructed that allows pressure measurement along the length of the test cell to confirm this hypothesis.

Flow visualization experiments using Computed Tomography further confirm the theoretical and experimental results. The results show fluid motion within the flow channel consistent with expectations. Fluid motion form the bounding surface to the middle of the channel is evident. Additionally, fluid displacement is not uniform along the length of the channel due to the cross-flow required for fluid to pass through the spacer openings.

References

A.L. Ahmad, K.K. Lau, Impact of different spacer filaments geometries on 2D unsteady hydrodynamics and concentration polarization in spiral wound membrane channel, J. Membr. Sci. 286 (2006) 77.

J. Balster, I. Punt, D.F. Stamatialis, M. Wessling, Multi-layer spacer geometries with improved mass transport, J. Membr. Sci. 282 (2006) 351.

J. Balster, D.F. Stamatialis, M. Wessling, Membrane with integrated spacer, J. Membr. Sci. 360 (2010) 185.

C. Bartels, M. Hirose, H. Fujioka, Performance advancement in the spiral wound RO/NF element design, EDS Conference proceedings, April 2007, Halkidiki, Greece.

Z. Cao, D.E. Wiley, A.G. Fane, CFD simulation of net-type turbulence promoters in a narrow channel, J. Membr. Sci. 185 (2001) 157.

A.P. Colburn, Heat transfer and pressure drop in empty, baffled and packed tubes. I. Heat transfer in packed tubes, Ind. Eng. Chem. 23 (1931) 910.

A.R. DaCosta, A.G. Fane, C.J.D. Fell, A.C.M. Franken, Optimal channel spacer design for ultrafiltration, J. Membr. Sci. 62 (1991) 275.

A.R. DaCosta, A.G. Fane, D.E. Wiley, Ultrafiltration of whey protein solutions in spacer-filled channels, J. Membr. Sci. 76 (1993) 245.

D. Dendukuri, S. K. Karode, A. Kumar, Flow visualization through spacer filled channels by computational fluid dynamics-II: improved feed spacer designs, Journal of Membrane Science 249 (2005) 41.

G.A. Fimbres-Weihs, D.E. Wiley, Numerical study of mass transfer in three-dimensional spacer-filled narrow channels with steady flow, J. Membr. Sci. 306 (2007) 228.

G.A. Fimbres-Weihs, D.E. Wiley, Numerical study of two-dimensional multi-layer spacer designs for minimum drag and maximum mass transfer, J. Membr. Sci. 325 (2008) 809.

V. Geraldes, V. Semiao, M.N. de Pinho, The effect of the ladder-type spacers configuration in NF spiral-wound modules on the concentration boundary layers disruption, Desalination 146 (2002a) 187.

V. Geraldes, V. Semiao, M.N. de Pinho, Flow management in nanofiltration spiral wound modules with ladder-type spacers J. Membr. Sci. 203 (2002b) 87.

G. Guillen, E.M.V. Hoek, Modeling the impacts of feed spacer geometry on reverse osmosis and nano-filtration Processes, Chemical Engineering Journal 149 (2009) 22.

A. Iranshahi, Static Mixing Spacers for Spiral Wound Modules, Masters Thesis, University of Toledo, 2012

S.K. Karode, A. Kumar, Flow visualization through spacer filled channels by computational fluid dynamics I. Pressure drop and shear rate calculations for flat sheet geometry, Journal of Membrane Science 193 (2001) 69-84.

C.P. Koutsou, S.G. Yiantsios, A.J. Karabelas, Direct numerical simulation of flow in spacer-filled channels: Effect of spacer geometrical characteristics, J. Membr. Sci. 291 (2007) 53.

C.P. Koutsou, S.G. Yiantsios, A.J. Karabelas, A numerical and experimental study of mass transfer in spacer-filled channels: Effect of spacer geometrical characteristics and Schmidt number, J. Membr. .Sci. 326 (2009) 234.

K.K. Lau, M.Z. Abu Bakar, A.L. Ahmad, T. Murugesan, Effect of feed spacer mesh length ratio on unsteady hydrodynamics in 2D spiral wound membrane (SWM) channel, Ind. Eng. Chem. Res. 49 (2010) 5834.
L.G. Leal, Advanced Transport Phenomena, Cambridge University Press, New York, 2007.
F.B. Leitz, L. Marinicic, Enhanced mass transfer in electrochemical cells using turbulence promoters, J. Appl. Electrochem. 7 (1977) 473.
F. Li, G.W. Meindersma, A.B. de Haan, T. Reith, Optimization of non-woven spacers by CFD and validation by experiments, Desalination 146 (2002a) 209.
F. Li, G.W. Meindersma, A.B. de Haan, T. Reith, Optimization of commercial net spacers in spiral wound membrane modules, J. Membr. Sci. 208 (2002b) 289.
F. Li, G.W. Meindersma, A.B. de Haan, T. Reith, Experimental validation of CFD mass transfer simulations in flat channels with non-woven spacers, J. Membr. Sci. 232 (2004) 19.
F. Li, W. Meindersma, A.B. de Haan and T. Reith, Novel spacers for mass transfer enhancement in membrane separations, J Membr. Sci. 253 (2005) 1.
Y.L. Li, K.L. Tung, CFD simulation of fluid flow through spacer-filled membrane module: selecting suitable cell types for periodic boundary conditions, Desalination 233 (2008) 351.
W.G. Light, T.V. Tran, Improvement of thin-channel design for pressure-driven membrane systems, Ind. Eng. Chem. Process Des. Dev. 20 (1981) 33.
E. Lyster, Y. Cohen, Numerical study of concentration polarization in a rectangular reverse osmosis membrane channel: Permeate flux variation and hydrodynamic end effects, J. Membr. Sci. 303 (2007) 140.
J.M. Miranda, J.B.L.M. Campos, Mass transfer in the vicinity of a separation membrane – the applicability of the stagnant film theory, J. Membr. Sci., 202 (2002) 137.
S.V. Polyakov, F.N. Karelin, Turbulence promoter geometry: its influence on salt rejection and pressure losses of a composite-membrane spiral wound module, J. Membr. Sci. 75 (1992) 205.
V.V. Ranade, A. Kumar, Comparison of flow structures in spacer-filled flat and annular channels, Desalination 191 (2006a) 136.
V.V. Ranade, A. Kumar, Fluid dynamics of spacer filled rectangular and curvilinear channels, J. Membr. Sci. 271 (2006b) 1.
G. Schock, A. Miquel, Mass transfer and pressure loss in spiral wound modules, Desalination, 64 (1987) 339.
F. Schwager, P.M. Robertson, N. Ibl, The use of eddy promoters for the enhancement of mass transport in electrodialysis cells, Electrochim. Acta 25 (1980) 1655.
J. Schwinge, D.E. Wiley, A.G. Fane, G. Gunther, Characterization of a zigzag spacer for ultrafiltration, J. Membr. Sci. 172 (2000) 19.
J. Schwinge, D.E. Wiley, D.F. Fletcher, Simulation of flow around spacer filaments between channels walls. Part I. Hydrodynamics, Ind. Eng. Chem. Res. 41 (2002a) 2977.
J. Schwinge, D.E. Wiley, D.F. Fletcher, Simulation of flow around spacer filaments between channels walls. Part II. Mass transfer, Ind. Eng. Chem. Res. 41 (2002b) 4879.
J. Schwinge, D.E. Wiley, D.F. Fletcher, Simulation of flow around spacer filaments between channels walls, Unsteady flows, Ind. Eng. Chem. Res. 42 (2003) 4962.
J. Schwinge, P.R. Neal, D.E. Wiley, D.F. Fletcher, A.G. Fane, Spiral wound modules and spacers. Review and analysis, J. Membr. Sci. 242 (2004) 129.

J.S. Shen, R.F. Probstein, Turbulence promotion and hydrodynamic optimization in an ultrafiltration process, Ind. Eng. Chem. Process Des. Dev. 18 (1979) 547.
Shrivastava, S. Kumar, E.L. Cussler, Predicting the effect of membrane spacers on mass transfer, Journal of Membrane Science 323 (2008) 247.
D.G. Thomas, W.L. Griffith, R.M. Keller, The role of turbulence promoters in hyperfiltration plant optimization, Desalination 9 (1971) 33.
D.E. Wiley, D.F. Fletcher, Computational fluid dynamics modeling of flow and permeation for pressure-driven membrane processes, Desalination 145 (2002) 183.
D.E. Wiley, D.F. Fletcher, Techniques for computational fluid dynamics modelling of flow in membrane channels, J. Membr. Sci. 211 (2003) 127.